Sustainable Food Technology

ROYAL SOCIETY OF CHEMISTRY

PAPER

Published on 26 October 2026
Licensed under CC-BY 4.0

Check for updates

Cite this: DOI: 10.1039/d6fb00278a

Waste-to-nanomedicine: scalable production of apple pomace nanovesicle-enriched fractions as nanocarriers for hydrophobic bioactives at the intestinal epithelial interface

Edoardo Bertania, †[a] Angelo Modena,†[a] Elia Bari, *[a] Erika Del Grosso,[a] Simona Turi, [bc] Rossana Rossi,[c] Saleh Hamed,[c] Yassine Jaouhari,[a] Fabiano Travaglia,[a] Guillaume Gilliard,‡[d] Melissa Ann Graewert,[e] Claudia Moscheni,[f] Valeria Rondelli, [d] Maria Luisa Torre,[ag] Anastasiia Murmiliuk §[d] and Dario Di Silvestre§[c]

Plant-derived extracellular vesicles (EVs) are emerging as promising nanocarriers for the stabilization and delivery of hydrophobic bioactive compounds, owing to their biocompatibility and membrane-mimetic properties. In this study, nanovesicle-enriched fractions were isolated from dry apple press residues, an agri-food byproduct. The resulting EV-enriched fraction exhibited a heterogeneous size distribution (100–500 nm), a characteristic vesicular morphology determined by transmission electron microscopy (TEM), and a lipid bilayer with adsorbed protein corona determined by Attenuated Total Reflectance-Fourier Transform Infrared (ATR-FTIR) and Small-Angle X-ray Scattering (SAXS). Moreover, proteomic analysis identified 588 non-redundant proteins, mainly linked to metabolic pathways, membrane trafficking, and structural stabilization. The EV-enriched fraction exhibited dose-dependent antioxidant and anti-tyrosinase activities and cytocompatibility in Caco-2 cells. Ursolic acid (UA), a poorly water-soluble bioactive compound, was successfully associated with the nanovesicle-enriched fraction by sonication. In Caco-2 Transwell® experiments, nanovesicle association increased the amount of UA recoverable from the donor medium relative to free UA, consistent with improved apparent dispersibility. However, UA remained below the lower limit of quantification in the receiver compartment for both formulations, indicating no detectable transepithelial transport under the tested conditions. In complementary Caco-2 exposure experiments, free UA showed a time-dependent increase in the cell-associated fraction, whereas UA administered with the nanovesicle-enriched fraction remained markedly lower. Overall, these findings indicate that apple pomace-derived nanovesicle-enriched fractions primarily act as stabilizing extracellular nanocarriers that maintain hydrophobic bioactives in a recoverable dispersed state, rather than promoting their epithelial association or transepithelial permeation. These properties support their potential use for local delivery of poorly water-soluble compounds at the intestinal epithelial interface.

Received 20th July 2026
Accepted 25th October 2026

DOI: 10.1039/d6fb00278a

rsc.li/susfoodtech

[a]University of Piemonte Orientale, Department of Pharmaceutical Sciences, 28100 Novara, Italy. E-mail: elia.bari@uniupo.it

[b]University of Padova, Department of Biomedical Sciences, 35131 Padova, Italy

[c]National Research Council, Institute for Biomedical Technologies, 20054 Segrate, Italy

[d]University of Milan, Department of Medical Biotechnology and Translational Medicine, 20054 Segrate, Italy

[e]European Molecular Biology Laboratory, Hamburg Unit, 22607 Hamburg, Germany

[f]University of Milan, Department of Biomedical and Clinical Sciences, 20157 Milan, Italy

[g]PharmaExceed S.r.l, 27100 Pavia, Italy

† Edoardo Bertania and Angelo Modena contributed equally as co-first authors.

‡ Current address: University of Picardie Jules Verne, Unité de génie enzymatique et cellulaire, UMR 7025, 80039 Amiens, France.

§ Dario Di Silvestre and Anastasiia Murmiliuk contributed equally as co-last authors.

¶ Current address: University of Liège, Department of Chemistry, UR Molecular Systems, 4000 Liège, Belgium.

© 2026 The Author(s). Published by the Royal Society of Chemistry

Sustainability spotlight

This work demonstrates a sustainable and scalable strategy for valorizing apple pomace, an abundant agri-food byproduct, as a source of naturally derived extracellular vesicles for the delivery of poorly water-soluble bioactive compounds. By combining waste-stream upcycling with tangential flow filtration and freeze-drying, the proposed approach supports the conversion of food-processing residues into stable, value-added functional nanomaterials while enabling process scalability. The resulting vesicles improve the dispersibility and intestinal retention of hydrophobic bioactives, expanding their potential use in functional food and nutraceutical applications. This strategy contributes primarily to SDG 12 (Responsible Consumption and Production) and SDG 9 (Industry, Innovation and Infrastructure) by promoting circular resource use and scalable sustainable food-processing technologies.

1. Introduction

Extracellular vesicles (EVs) are lipid bilayer-enclosed particles that lack a nucleus and are unable to replicate.[1,2] They are secreted into the extracellular space by both prokaryotic and eukaryotic cells, including those of animals and plants, through mechanisms that appear at least partially conserved across kingdoms.[3] Plant-derived EVs can be isolated from various organs, such as fruits, roots, seeds, leaves, and exudates.[4] Although plant- and animal-derived EVs share certain structural and functional similarities, they differ in size, composition, and cargo. In particular, plant-derived EVs are generally larger, with diameters ranging from 50–500 nm, and their molecular content, including proteins, lipids, and RNA, is distinguished by the presence of secondary metabolites.[5,6]

From an application perspective, plant-derived EVs are currently being investigated along two complementary directions. First, their endogenous molecular cargo may confer intrinsic biological activities: preclinical studies have reported anti-inflammatory and antioxidant effects,[7–20] regenerative and anticancer activity,[21–36] and modulation of the gut microbiota.[37–43] These activities are attributed to the combined contribution of vesicular lipids, small RNAs, and plant secondary metabolites, and are retained after isolation, indicating that the vesicular fraction itself – rather than the source extract – is the active entity.[44,45] Second, their lipid bilayer, biocompatibility, and capacity to accommodate exogenous molecules have stimulated their development as natural nanocarriers for drug delivery.[46–48] In this respect, plant-derived EVs offer an amphiphilic architecture that enables the encapsulation of both hydrophilic and hydrophobic molecules,[49] colloidal stability in aqueous media, and the ability to interact with biological interfaces, all properties relevant to keeping poorly water-soluble compounds in a dispersed and bioavailable state.[50,51] Their internalization efficiency also appears to exceed that of synthetic liposomes, likely because their lipid composition closely mimics physiological cell membranes.[52] Compared with liposomes or animal-derived EVs, they additionally raise fewer safety and immunogenicity concerns,[44] are more resistant to gastrointestinal digestion,[50,53] and are more amenable to cost-effective large-scale production[51,54] – a combination that makes the oral route a particularly plausible application scenario. Nevertheless, the physicochemical basis of their interaction with lipid membranes, and consequently their effects on epithelial association, uptake, and transepithelial transport, remain poorly defined.[47,50,51] Accordingly, several studies have explored the use of plant-derived EVs for drug delivery, including the encapsulation of active pharmaceutical ingredients such as doxorubicin,[55–57] paclitaxel,[58] and RNA molecules.[59–64] An additional compound that would benefit from association with plant-derived nanovesicular carriers is ursolic acid (UA), a naturally occurring pentacyclic triterpenoid found in several fruits and medicinal plants, including apple peel.[65] UA has attracted considerable interest because of its reported biological activities, including anti-inflammatory and antioxidant properties.[66–68] However, its pharmaceutical exploitation is strongly limited by unfavorable biopharmaceutical properties. UA exhibits very low aqueous solubility and limited intestinal permeability and is consequently characterized by poor oral bioavailability.[68–70] These features make UA a particularly informative model cargo for evaluating delivery systems intended for poorly water-soluble bioactives, and a suitable probe for assessing whether an EV-enriched fraction can associate with a highly lipophilic compound, maintain it in a dispersed and accessible state in an aqueous environment, and modulate its interaction with the intestinal epithelial interface.

Beyond these biological considerations, the clinical translation of plant-derived EVs depends on three process-related bottlenecks. The first is the choice of an abundant and readily available source material. EVs can be recovered from agri-food wastes generated during industrial food processing,[71] which would decouple production from dedicated cultivation, but applications in this field remain limited, with only one reported example of EVs derived from olive vegetation water.[72] Apple press residues are an attractive candidate in this respect, being produced in large and consistent volumes by the juice industry, available as a byproduct of an established supply chain, and otherwise destined for low-value uses. The second bottleneck is isolation. Techniques initially developed for animal-derived EVs, such as ultracentrifugation, polymer precipitation, and immunoaffinity purification, have been adapted for plants,[73–75] yet scalable, standardized, and Good Manufacturing Practice (GMP)-compliant protocols are still lacking, and comprehensive characterization tools – including high-throughput omics and surface marker profiling – remain to be optimized for plant-derived vesicles.[18,75,76] The third is stability: EV suspensions are prone to aggregation and cargo loss during storage, so a downstream step compatible with long-term preservation, such as freeze-drying, is required before any realistic pharmaceutical use.

Based on these premises, the present study aims to isolate nanovesicles from dry apple press residues and to evaluate their potential as both biologically active substances and drug delivery systems. To this end, EV-enriched fractions were isolated using a tangential flow filtration (TFF)-based process designed to be

© 2026 The Author(s). Published by the Royal Society of Chemistry

compatible with GMP requirements and subsequently freeze-dried to ensure long-term stability. Apple-derived nanovesicles were characterized for protein and lipid content, particle size, physico-chemical properties, and *in vitro* biological activity. Their suitability as delivery vehicles was assessed through interaction studies with cell membranes. Following confirmation of cyto-compatibility in Caco-2 cells, apple-derived nanovesicles were associated with UA *via* sonication, and their ability to improve UA dispersibility and modulate its interaction with the intestinal epithelial interface was evaluated using a Caco-2 Transwell® model together with complementary cell-association experiments.

2. Materials and methods

2.1 Materials

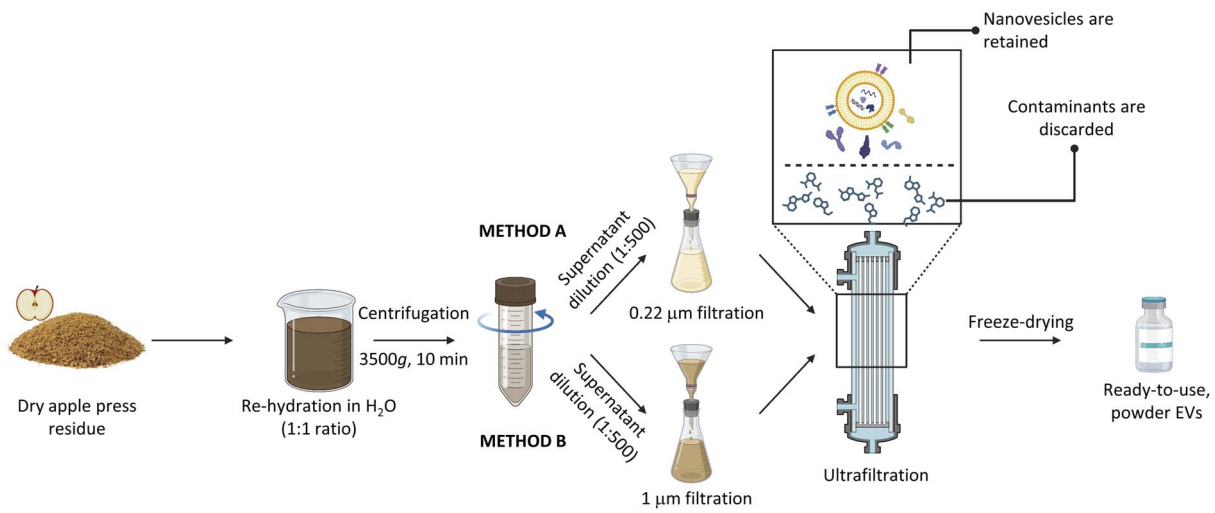
Acetone, acetonitrile, dimethylsulfoxide (DMSO), formic acid, hydrogen peroxide (H_2O_2), methanol, trifluoroacetic acid (TFA), and uranyl acetate solution were purchased from Carlo Erba Reagents, Milan, Italy. 3-(4,5-dimethylthiazol-2-yl)-2,5-diphenyltetrazolium bromide (MTT), bovine serum albumin (BSA), mannitol, Nile red, and phosphatidylcholine (PC) were purchased from Merck, Milan, Italy. Cell culture media and reagents, including phosphate-buffered saline (PBS), were purchased from Euroclone, Milan, Italy. Cells were purchased from Promocell, Heidelberg, Germany. Dried apple pomace was kindly donated by Plantex sas, Groppello Cairoli, Pavia, Italy. UA was purified by crystallization and vacuum filtration from an acetonic extract of *Ilex paraguariensis* and obtained as a white powder. 1,2-dimyristoyl-*sn*-glycero-3-phosphocholine (DMPC), 1,2-dioleoyl-*sn*-glycero-3-phosphocholine (DOPC), sphingomyelin from chicken egg yolk, and cholesterol were purchased from Merck, Milan, Italy, and used without further purification. RapiGest SF was from Waters Corporation, Milford, MA, USA; sequencing-grade modified trypsin was from Promega, Madison, WI, USA, and LC-MS grade water was from LC-MS Ultra CHROMASOLV™, Honeywell Riedel-de Haen™, Muskegon, MI, USA.

2.2 Isolation of apple-derived EV-enriched fractions

Dry apple press residue was rehydrated in ultrapure water (1 : 1 ratio) under static conditions at 4 °C for 24 h and centrifuged at 3500×*g* for 10 min; the supernatant was diluted with ultrapure deionized water (final solid ratio of 1 : 500), filtered through 70 μm filters, and then filtered 0.22 μm (method A) or filtered 1 μm (method B) to remove pectins before being processed through TFF, as previously reported.[77] The KrosFlo® Research 2i system (Spectrum Laboratories, Milan, Italy), equipped with a modified polyethersulfone membrane with a 300 kDa molecular weight cut-off (Spectrum Laboratories, Milan, Italy), was used. Following concentration (final volume = 25% of the initial volume), the samples were dialyzed using sterilized and ultrapure water as a buffer. During both steps, the shear rate of the feed stream was kept between 2000 s^{-1} and 6000 s^{-1}, while the *trans*-membrane pressure remained within 2.1–3.5 psi. Samples were added with mannitol (0.5% w/v), frozen at −80 °C, and freeze-dried (Christ Epsilon 2-16D LSCplus, Christ GmbH, Christ, Osterode am Harz, Germany) at 8 × 10^{-1} mbar and −50 °C for 72 h following the procedure reported in ref. 77 (Scheme 1). The obtained freeze-dried nanovesicle-enriched fractions were stored at −20 °C until use (12 months maximum). Production runs were performed using material obtained from three independent batches of dry apple pomace. For each production run, the amount of starting dry pomace, total process water consumption, feed volume, final retentate volume, membrane area, processing time, *trans*-membrane pressure, and permeate flux were recorded. The dry-product yield was also calculated as the mass of freeze-dried nanovesicle-enriched material per gram of starting dry apple pomace; protein and lipid yields were similarly normalized to the mass of starting dry pomace (Table S1).

2.3 Characterization of apple-derived nanovesicles

The characterization was performed on both fresh and freeze-dried EV-enriched fractions (obtained with methods A and B), as detailed below.



Scheme 1 Isolation process of apple-derived nanovesicles.

© 2026 The Author(s). Published by the Royal Society of Chemistry

2.3.1 Protein and lipid content. Nanovesicles obtained with method A or B were characterized for protein and lipid content.

Proteins were quantified using the Micro-BCA Protein Assay Kit (Thermo Fisher Scientific, Milan, Italy) following the internal standard method. Briefly, increasing amounts of BSA were added to the sample, achieving a final concentration range between 0 and 100 μg mL^{-1}. Subsequently, 100 μL of each concentration was plated in triplicate into a 96-well plate, followed by the addition of 100 μL of reagent prepared according to the manufacturer's instructions. After 2 h of incubation at room temperature, absorbance was measured at 562 nm using a multiwell plate reader (Victor Nivo, PerkinElmer, Waltham, MA, USA). The initial unknown protein concentration in the sample was determined using a linear function ($R^2 = 0.99$).

Lipid quantification followed a similar approach, using the procedure described by Bari *et al.*[77] with some modifications. Increasing amounts of PC were added to the sample, achieving a final concentration range between 0 and 20 μg mL^{-1}. In a 96-well plate, 90 μL of each concentration was plated in triplicate. Then, 10 μL of Nile red solution (1 mg mL^{-1} dissolved in acetone, diluted 100× in ultrapure deionized water) was added to each well. Wells where 10 μL of deionized water was added instead of Nile red served as blanks. The fluorescence was measured (excitation 530/25 nm and emission 645/40 nm) using a multiwell plate reader (Victor, PerkinElmer, Waltham, MA, USA). The initial unknown lipid concentration in the sample was determined using a linear function ($R^2 = 0.98$).

2.3.2 Nanovesicle particle size. Particle size and size distribution of fresh and freeze-dried nanovesicles were determined by exploiting the nanoparticle tracking analysis (NTA) technology using a NanoSight NS300 instrument (Malvern Instruments, Malvern, UK) equipped with a $\lambda = 405$ nm laser. Fresh samples were directly diluted 1 : 100 in ultrapure water, while freeze-dried ones were analyzed after being dispersed at 1 mg mL^{-1} and diluted 1 : 100 in ultrapure water. All analyses were conducted at 25 °C with a 90-degree refractive angle. Data were processed using the NTA 3.0 software (Malvern Instruments, Malvern, UK) to determine the particle size distribution in number and nanovesicle concentration. Each analysis was performed in quintuplicate.

The size distribution was also measured with a custom dynamic light scattering (DLS) apparatus[78] at 90° using an Nd:YAG laser source of $\lambda = 532$ nm. Measurements were performed at 25 °C on samples in quartz cuvettes. The measurements were repeated 10 times per sample and analyzed by the CONTIN algorithm, showing both the intensity and number of weighted distributions.

2.3.3 Nanovesicle morphology by transmission electron microscopy (TEM). Nanovesicles were characterized using negative stain electron microscopy. Briefly, a 10 μL drop of sample dispersion was placed on parafilm, and a 150-mesh formvar-carbon-coated electron microscopy grid was left in contact with the sample for 10 min. Then, the grid was washed in separate 40 μL drops of distilled water for 1 min. Finally, the grid was placed on a 40 μL drop of 1% uranyl acetate solution for 10 min in dark conditions, followed by blotting to remove excess liquid. Grids were observed with an EM-109 transmission electron microscope (Carl Zeiss, Oberkochen, West Germany) with an Olympus Mega View G2 TEM CCD Camera System. All measurements were manually performed using the integrated TEM imaging Platform iTEM (Olympus Soft Imaging Solutions, Münster, Germany) on randomly acquired micrographs. The identification of nanovesicles was carried out at high magnification (≈85 000×).

2.3.4 Physico-chemical and membrane interaction studies. Small-Angle X-ray Scattering (SAXS) and Fourier-Transform Infrared Spectroscopy (FTIR) were applied to investigate nanoscale structure and mean composition of the EV-enriched fractions upon different purification steps: at the end of TFF processing and after additional ultracentrifugation performed using the centrifuge (Beckman Coulter, Brea, CA, USA) at 35 000 rpm for 30 min at 4 °C, to further separate the nanovesicles from proteins and sugars in solution. SAXS experiments were performed on the high-brilliance beamline ID02 equipped with an Eiger2 4M detector, X-ray energy of 12.23 keV (wavelength of 1.013 Å) at the European Synchrotron Radiation Facility (Grenoble, France) in 0.2 cm flow-through quartz capillaries at a sample-to-detector distance of 1.5 m. The empty capillary and background subtraction were performed using SAXS utilities software.[79] The raw data from the ID02 beamline at ESRF are available at https://doi.esrf.fr/10.15151/ESRF-ES-1837447272 and https://doi.esrf.fr/10.15151/ESRF-ES-1925860640. SAXS experiments for nanovesicle interaction with biomimetic membranes were performed using the EMBL P12 beamline of the storage ring PETRA III (DESY, Hamburg).[80] The sample (40 μL) was loaded into the flow-through capillary at 37 °C using a sample changer. All measurements were performed at a wavelength of 0.124 nm with an exposure time of 0.1 s, and the scattered photons were detected using a PILATUS 6 M detector at a sample-to-detector distance of 3 m. 40 frames were collected and normalized to the transmitted beam for each sample to make corrections for variations in the sample thickness and beam flux. The data reduction was performed using the SASFLOW pipeline.[81] The scattering from water was subtracted to remove the solvent background. The scattering profiles are presented on an absolute intensity scale, calibrated using water.

FTIR experiments were performed using the Attenuated Total Reflectance (ATR-FTIR) technique by thin film deposition onto a ZnSe crystal with a Nicolet iS50 apparatus from Thermo Fisher Scientific, San Josè, CA, USA. The background signal was collected for an empty crystal at room temperature in the wavenumber range 4000–700 cm^{-1} and was subtracted from the sample signal. For the measurements, 100 μL of nanovesicles in aqueous solution were distributed over the crystal, the solvent was evaporated in the oven for 1 h at 40 °C, and the measurement was performed at room temperature. The ATR-FTIR spectra were analyzed using OriginLab software for baseline correction, peak finding, peak integration, and peak deconvolution by the Bigaussian function.

Interaction with model membranes, to deepen the details of nanovesicles' interaction with the plasma membrane, was also

 © 2026 The Author(s). Published by the Royal Society of Chemistry

studied by SAXS. Model membranes were prepared by hydration of lipid films consisting of 1,2-dimyristoyl-*sn*-glycero-3-phosphocholine (DMPC), 1,2-dioleoyl-*sn*-glycero-3-phosphocholine (DOPC), DMPC : Sphingomyelin : Cholesterol (DOPC : SM : Chol) or DOPC : Sphingomyelin : Cholesterol (DOPC : SM : Chol) mixture (molar ratio 1 : 0.3 : 0.05). Membranes were extruded using a 100 nm polycarbonate membrane 51 times at 37 °C to obtain large unilamellar vesicles (LUVs) and diluted to a final concentration of 10 mg mL^{-1}. The nanovesicles were added to the LUVs and incubated at 37 °C for 2 h prior to SAXS measurements.

2.3.5 Antioxidant, anti-elastase, and anti-tyrosinase activities. The ROS-scavenging, anti-elastase, and anti-tyrosinase activities of freeze-dried EV-enriched fractions were evaluated as previously reported.[82] Samples were tested at various final concentrations in the reaction mix (21, 10, 5, 2, 1, and 0.5 mg mL^{-1}). Absorbance for all assays was measured using a multi-well plate reader (Victor Nivo, PerkinElmer, Waltham, MA, USA).

2.3.6 Cytocompatibility and oxidative protection evaluation on Caco-2 cells. The cytocompatibility of freeze-dried EV-enriched fractions was assessed on Caco-2 cells using the MTT assay. Caco-2 cells were seeded in a 96-well plate (3000 cells per well) and cultured for 72 h at 37 °C and 5% CO_2. Then, cells were treated with 100 μL of culture medium containing the samples at concentrations of 75, 50, 25, and 5 mg mL^{-1}. After 24 h of incubation, cell metabolic activity was evaluated using the MTT assay, as previously described.[82]

To assess the protective effect against oxidative stress, Caco-2 cells were treated with the samples for 24 h and subsequently exposed to 1 mM H_2O_2 for another 24 h. Cells not incubated with H_2O_2 were considered as controls. After 24 h, an MTT test was performed to assess the cell metabolic activity.[82] Each experiment was performed in triplicate.

2.4 Proteomic analysis

2.4.1 Sample preparation. Samples collected at the end of ultracentrifugation and before cryoprotectant addition (350 μL) were concentrated to 50 μL using a vacuum concentrator at 60 °C (Savant Instruments, Farmingdale, NY, USA). Protein concentration was determined using the QUBIT Protein Assay kit (Life Technologies Corporation, Thermo Fisher Scientific Inc., Eugene, ORE, USA). A total of 6 μg of protein was treated with RapiGest SF at a final concentration of 0.25% w/v. Following incubation at 95 °C for 20 min, samples were cooled to room temperature and centrifuged at 2200×*g* for 10 min. Enzymatic digestion was then carried out using sequencing-grade modified trypsin at an enzyme/substrate ratio of 1 : 50 w/w at 37 °C overnight. The next morning, an additional aliquot of enzyme was added (enzyme/substrate ratio of 1 : 100 w/w). The enzymatic reaction was chemically stopped after 3 h by acidification with TFA 0.5% v/v, followed by incubation at 37 °C for 45 min and centrifugation at 13 000 rpm for 10 min in order to remove hydrolyzed RapiGest SF by-products. The tryptic peptides were desalted using C-18 spin columns (G-Biosciences, St. Louis, MO, USA), according to the manufacturer's protocol, concentrated in a vacuum concentrator at 60 °C, and finally resuspended in 0.1% v/v formic acid in LC-MS grade water at a final concentration of 0.1 μg μL^{-1}.

2.4.2 LC–MS analysis. The peptide mixtures obtained after trypsin digestion were analyzed using the Eksigent nanoLC-Ultra® 2D System (Eksigent, AB SCIEX Dublin, CA, USA) combined with the cHiPLC®-nanoflex system (Eksigent) in trap-elute configuration. Samples were first loaded on the cHiPLC trap (200 μm × 500 μm ChromXP C18-CL, 3 μm, 120 Å) and washed with 0.1% v/v formic acid in water at a flow rate of 3 μL min^{-1} for 10 min under isocratic conditions. Automatic switching of the cHiPLC ten-port valve then eluted the trapped mixture on a nano cHiPLC column (75 μm × 15 cm ChromXP C18-CL, 3 μm, 120 Å), using a 105 min gradient of eluent B (eluent A, 0.1% v/v formic acid in water; eluent B, 0.1% v/v formic acid in acetonitrile), at a flow rate of 300 nL min^{-1}. The gradient profile was as follows: from 5–10% B in 3 min, 10–30% B in 77 min, 30–95% B in 15 min, and holding at 95% B for 10 min. Both the trap and column were maintained at 35 °C to ensure consistent elution times.

Mass spectra were acquired using an Orbitrap Exploris 120 mass spectrometer (Thermo Fisher Scientific, San Josè, CA, USA), equipped with an EASY-Spray ion source (Thermo Fisher Scientific, San Josè, CA, USA). Ionization was achieved using an EASY-Spray Emitter (Thermo Fisher Scientific, San Josè, CA, USA; nanoflow 7 μm ID Transfer Line 20 μm × 50 cm) held to 1.6 kV, and the ion transfer capillary was held at 220 °C. Data-dependent acquisition was performed, acquiring precursor ions in the *m*/*z* range of 375–1250 with a resolution (at *m*/*z* 200) of 60 000 FWHM (full width at half maximum). Precursor fragmentation was carried out at a resolution (at *m*/*z* 200) of 15 000 FWHM, using a higher-energy collisional dissociation (HCD) method with a normalized collision energy set to 30 eV and a dynamic exclusion of 20 s. MS and MS/MS data were acquired in profile and centroid modes, respectively, using positive polarity and isotope exclusion enabled. The isolation width was set to 2 *m*/*z*, and the first mass was set to 120 *m*/*z*. Mass spectrometer scan functions and high-performance liquid chromatography solvent gradients were controlled by the Xcalibur v.4.4 (Thermo Fisher Scientific, CA, USA) and Eksigent Control Software v.4.3 (Eksigent, part of AB SCIEX, Dublin, CA, USA), respectively.

2.4.3 Raw data processing. The experimental MS/MS spectra were matched against the *in silico* tryptic peptide sequences of the *Malus domestica* protein database (45 436 protein entries) retrieved from UNIPROT (September 2024). Data processing was performed by Proteome Discoverer 2.5 software, based on the SEQUEST HT algorithm. The following search parameters were applied: (i) parent mass tolerance = 10 ppm, (ii) peptide fragment mass tolerance = 0.05 Da, (iii) missed cleavage sites per peptide = 3. The percolator node was employed with a target-decoy strategy to achieve a final false discovery rate (FDR) ≤ 0.01 (strict) based on *q*-values, considering a maximum ΔCN of 0.05. Finally, only peptides with a minimum peptide length of 4 amino acids, confidence "Medium", and rank 1 were retained for subsequent analyses.

© 2026 The Author(s). Published by the Royal Society of Chemistry

2.4.4 Functional analysis. The identified proteins were managed using the Biostrings R library.[83] To reduce redundancy, pairwise global alignments were performed using the Needleman–Wunsch algorithm with the BLOSUM62 substitution matrix and gap penalties of 10 for opening and 0.5 for extension. The percent identity metric (PID2) was calculated to evaluate alignment similarity, and a 0.90 threshold was applied to flag sequences with identities above this level as redundant.[84] Owing to the limited *Malus domestica* functional annotations, the characterized protein profiles were functionally evaluated using the *Arabidopsis thaliana* proteome as a reference. To generate a rank list of the most abundant proteins in the analyzed samples, the average peptide spectrum matches (PSMs) of each protein were normalized according to the formula:

$$n\mathrm{PSM} = \frac{\mathrm{PSM}}{\mathrm{MW}} \times 110$$

where MW represents the molecular weight of a given protein, and 110 is the average molecular weight of an amino acid. The Functional Annotation Tool of the DAVID database was used to extract the most enriched molecular functions, biological processes, cellular components, and KEGG pathways; enrichment criteria were set as: count > 5 and $p < 0.01$.[85]

2.5 Nanovesicle loading with UA and characterization

2.5.1 Nanovesicle loading. UA was solubilized in DMSO (1 mg mL^{-1}) and then incubated with nanovesicles (obtained using method B) at increasing UA : EV ratios of 1 : 1, 1 : 2, 1 : 5, and 1 : 10, with nanovesicles quantified based on lipid content (μg). To facilitate the loading of UA into nanovesicles, the samples were placed in an ultrasonic bath and sonicated for 1 h on ice at 4 °C. Finally, the UA-loaded nanovesicles were subjected to static dialysis using membranes with a 3.5 kDa cut-off (Spectrum Laboratories, Milan, Italy) against distilled water for 72 h at room temperature.

2.5.2 Quantification of UA. The amount of UA recovered in association with the nanovesicle-enriched fraction after dialysis, recovered from the dialysis membrane, or detected in the dialysis medium was determined using a Q-Exactive Plus UHMR Hybrid Quadrupole Orbitrap™ Mass Spectrometer equipped with a Vanquish™ Duo UHPLC system (Waltham, MA, USA). Prior to LC-MS/MS analysis, the samples were quantitatively transferred into 10 mL volumetric flasks using methanol. The original sample containers were washed three times with 1 mL of methanol, and the combined extracts were brought to a final volume of 10 mL with methanol. Dialysis membranes were extracted with 5 mL of methanol, sonicated for 15 min at 30 °C, and quantitatively transferred to 10 mL volumetric flasks with methanol. Before LC-MS/MS analysis, samples were sonicated and centrifuged. Chromatographic analyses were conducted using a Kinetex® C18 column (2.6 μm, 100 Å, 150 × 2.1 mm). The column temperature was maintained at 40 °C, and the mobile phases used were H_2O with 0.1% v/v formic acid (mobile phase A) and methanol with 0.1% v/v formic acid (mobile phase B). Elution was performed under isocratic conditions with 80% mobile phase B throughout the chromatographic run (0–10 min). The mobile phase flow rate was set at 0.400 mL min^{-1}, and the injection volume was 5 μL. The total analysis time for each sample was 10 min. Mass spectra were acquired in parallel reaction monitoring mode in the mass range of m/z 50–750 at m/z 457.368 (HCD 14). Ionization was achieved using a source ionization voltage of 3.50 kV, and the ion transfer capillary was held at 300 °C. The isolation width was set to 2 m/z. All data were extracted by Xcalibur Software v. 3.1 (Thermo Fisher Scientific, CA, USA). The analytical method showed linearity over the concentration range of 0.015–1.5 μg mL^{-1}. The lower limit of quantification (LOQ) for UA was 0.015 μg mL^{-1}.

The encapsulation efficiency (EE%) of UA in nanovesicles was operationally calculated as the percentage of the nominally added UA recovered in association with the nanovesicle-enriched fraction after dialysis using the following formula:

$$\mathrm{EE\%} = \frac{\varepsilon\mathrm{gUA_{EVs}}}{\varepsilon\mathrm{gUA_{EVs}} + \varepsilon\mathrm{gUA_{membrane}} + \varepsilon\mathrm{gUA_{water}}} \times 100$$

where $\mu\mathrm{gUA_{EVs}}$ is the amount of UA recovered from the nanovesicle-containing fraction, $\mu\mathrm{gUA_{membrane}}$ is the amount recovered from the dialysis membrane, and $\mu\mathrm{gUA_{water}}$ is the amount recovered from the dialysis water.

To assess the analytical mass balance, overall UA mass recovery was calculated relative to the nominal UA amount according to:

$$\mathrm{UA\ recovery}(\%) = \frac{\varepsilon\mathrm{gUA_{EVs}} + \varepsilon\mathrm{gUA_{membrane}} + \varepsilon\mathrm{gUA_{water}}}{\varepsilon\mathrm{gUA_{nominal}}} \times 100$$

where $\mu\mathrm{gUA_{EVs}}$ is the amount of UA recovered from the nanovesicle-containing fraction, $\mu\mathrm{gUA_{membrane}}$ is the amount recovered from the dialysis membrane, $\mu\mathrm{gUA_{water}}$ is the amount recovered from the dialysis water, and $\mu\mathrm{gUA_{nominal}}$ is the nominal UA amount in the formulation.

The term "encapsulation efficiency" is used here as an operational formulation parameter and does not establish the precise localization of UA within the nanovesicles. Accordingly, this analytical measurement cannot distinguish UA incorporated within the vesicular lipid bilayer from UA strongly associated with the vesicle surface or other components co-recovered with the nanovesicle-enriched fraction.

2.5.3 Characterization of nanovesicles loaded with UA. Nanovesicles loaded with UA were characterized in terms of particle size (by NTA, as reported in Section 2.3.2), morphology (by TEM, as reported in Section 2.3.3), and physico-chemical properties (by SAXS and FTIR, as reported in Section 2.3.4).

2.5.4 Interaction study at the intestinal epithelial interface. A transport study of UA-EVs and free UA was carried out in Caco-2 cells, according to Sangsen *et al.*[86] Caco-2 cells were seeded on Transwell® inserts (24-well format, 3 μm pore size) and cultured until the formation of a differentiated epithelial monolayer. Transepithelial electrical resistance (TEER) values were measured before and at the end of the transport experiments to assess monolayer integrity; only monolayers showing TEER values higher than 300 Ω cm^2, consistent with the formation of a tight epithelial barrier,[87,88] were used for the experiments. The two formulations were administered at the same nominal UA dose of 10 μg mL^{-1} in the donor compartment. For free UA, the

© 2026 The Author(s). Published by the Royal Society of Chemistry

administered dose was calculated from the concentration of the prepared UA solution, whereas for the UA-EVs it was calculated from the measured UA content of the loaded preparation. Transport experiments were performed independently in the apical-to-basolateral and basolateral-to-apical directions. Samples were collected from the donor and receiver compartments after 15, 30, and 60 min, and UA was quantified as described in Section 2.5.2. UA concentration was not analytically determined immediately after dosing ($t = 0$).

2.5.5 Caco-2 cell-association study. To investigate the fate of UA at the cellular level, a complementary cell-association experiment was performed using Caco-2 cells cultured in 24-well plates. Cells were seeded at 10 000 cells per well and cultured for 5 days under standard conditions before treatment. Free UA and UA associated with the nanovesicle-enriched fraction were administered at the same nominal UA concentration of 10 μg mL^{-1} in a final volume of 1 mL per well, corresponding to a nominal dose of 10 μg UA per well. Experiments were performed in duplicate using two independent wells for each condition and time point, and cells were exposed to the formulations for 30, 60, or 120 min. At each time point, the culture supernatant was collected, and the cell monolayer was washed with PBS to recover residual and loosely associated UA. Cells were subsequently detached using trypsin/EDTA and collected as the cell-associated fraction. The culture supernatant, PBS wash, and cell-associated fractions were processed for LC-MS/MS analysis according to the sample-preparation procedure described in Section 2.5.2, and UA was quantified independently in each fraction. Each sample was analyzed in triplicate. The number of cells in each well was determined at the end of the experiment, and the amount of UA recovered in the cell-associated fraction was normalized to cell number and expressed as μg UA per 10^6 cells. Total UA recovery was calculated as the sum of the amounts quantified in the culture supernatant, PBS wash, and cell-associated fraction and expressed relative to the nominally administered dose (10 μg per well). Values below the LOQ were reported as BLQ.

2.6 Statistical analysis

Statistical analysis was performed using Statgraphics XVII (Statpoint Technologies, Inc., Warrenton, VA, USA) or GraphPad Prism version 8.0.2 (GraphPad Software, Boston, MA, USA), according to the tests indicated in the figure captions of the Results and discussion section. Statistical significance was set at $p < 0.05$.

3. Results and discussion

3.1 Isolation and characterization of nanovesicles from apple dry pomace

Apple-derived nanovesicles were successfully isolated from apple waste (press residue) using TFF and then freeze-dried. Preliminary filtration of the sample (using either a 0.22 μm or 1 μm filter) was necessary to remove pectin; without this step, pectin would accumulate on the filtration membrane, significantly reducing TFF efficiency. Feed volumes of 1.6–4.5 L, corresponding to a fixed 1 : 500 solid-to-water ratio, were concentrated fourfold to final retentates of 0.4–1.125 L over a 0.079 m^2 membrane, with processing times of 1.5–3.5 h. Transmembrane pressure remained within 2–3.5 psi throughout concentration and diafiltration, and permeate flux at 2 psi ranged from 151 to 271 L h^{-1} m^{-2}, indicating no marked progressive deterioration of membrane performance under the tested conditions (Table S1). The choice of TFF was primarily driven by process considerations. Unlike ultracentrifugation, which is intrinsically batch-based and difficult to implement at large feed volumes, TFF combines concentration and diafiltration in a membrane-based workflow that scales with the available filtration area – an advantage for plant-derived materials and agri-food byproducts, where large volumes must be handled. Here it was implemented within the standardized GMP-compliant workflow previously described.[77] The alternatives are less suitable: polymer-based precipitation co-isolates substantial non-vesicular material, while immunoaffinity purification remains difficult for plant-derived EVs given the current limitations in surface marker characterization.[18,73–76] TFF, however, should be regarded as an enrichment rather than a high-resolution purification step, since the molecular weight cut-off concentrates nanovesicles without fully separating them from co-isolated proteins, polysaccharides, and other macromolecules. Furthermore, scalability and GMP compatibility do not in themselves imply environmental sustainability. Total process water amounted to 625 L per kg of dry pomace (2–5.6 L per batch, Table S1), and the 72 h freeze-drying step is energy-demanding, although energy consumption was not quantified and no life-cycle assessment was performed. Water reduction, process intensification, and optimization of drying therefore remain targets for future development.

Following TFF processing and the lyophilization process, nanovesicles exhibited a round morphology (Fig. 1A).

Both methods A and B yielded heterogeneous nanovesicle populations with particle sizes ranging from 100 to 500 nm (Fig. 1B). Significantly larger mean diameters, d_{50} and d_{90} were observed for nanovesicles isolated using method B compared to those obtained with method A, whereas no significant differences were found in terms of mode and d_{10} (Fig. 1C). After lyophilization, the mean diameter, d_{50}, and d_{90} of nanovesicles isolated with method B decreased. In contrast, no significant differences were observed for mode and d_{10}, or between nanovesicles isolated with method A before and after lyophilization. This suggests that mannitol, acting as a cryoprotectant, effectively preserved vesicle integrity and prevented aggregation during freezing and dehydration. NTA data were in good agreement with the size distribution obtained from DLS. This analysis revealed, for nanovesicles prepared with method A, the presence of particles with an average size of 67 ± 29 nm from the number-weighted distribution, while for the ones prepared with method B, the average size was 140 ± 50 nm (Table S2). Nanovesicles isolated with method B contained particles of 100–190 nm, along with larger aggregates above 700 nm, while their average size was 140 ± 50 nm.

Protein and lipid contents were higher in EV-enriched fractions isolated using method B than in those obtained

© 2026 The Author(s). Published by the Royal Society of Chemistry

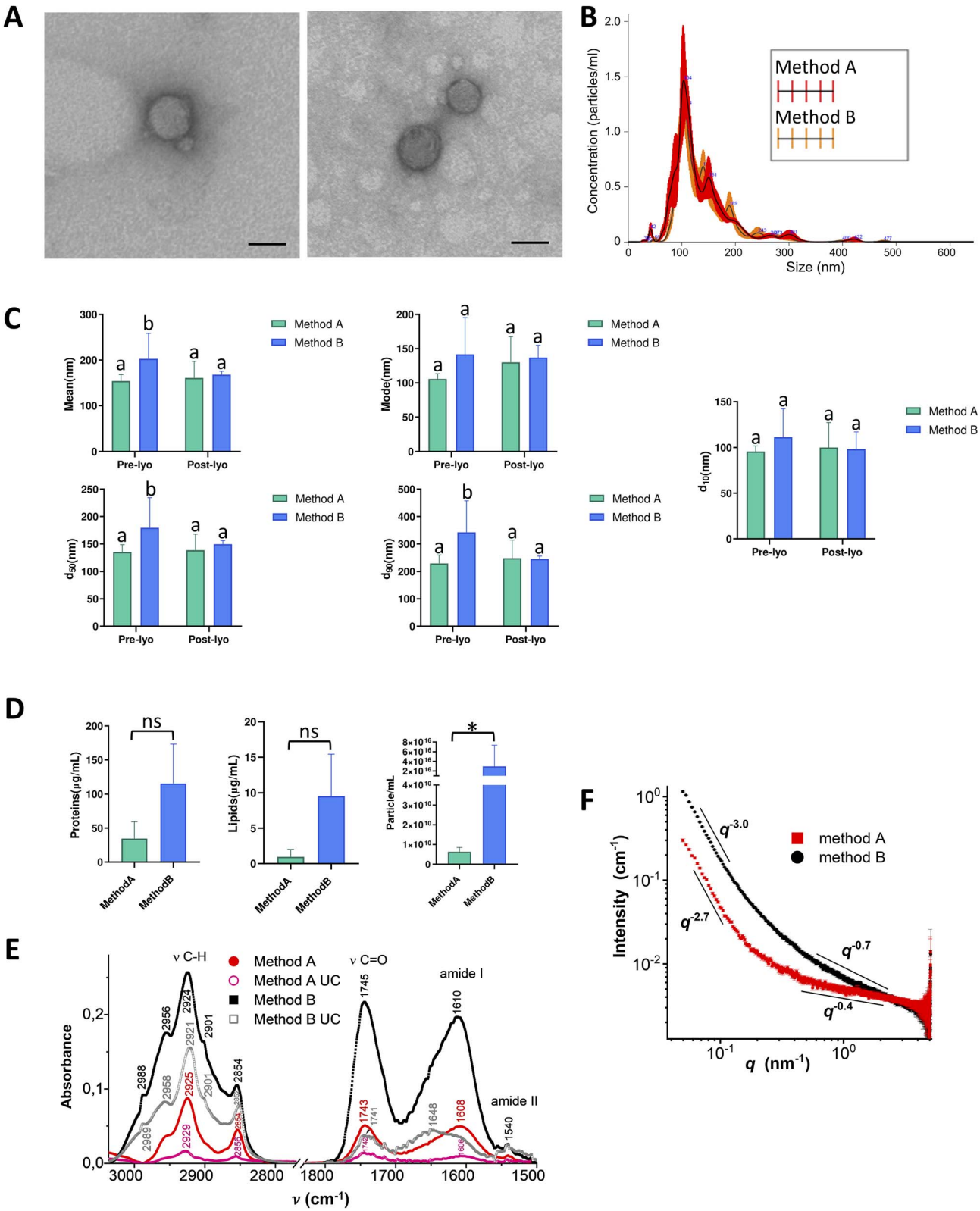


Fig. 1 (A) Representative TEM images of nanovesicles derived from apple isolated using method A (on the left) or method B (on the right). Scale bar: 50 nm. (B) Representative NTA graphs for nanovesicle batches prepared using method A (red curve) and method B (orange curve). The curves show the mean value (black line) ± standard deviation ($n = 5$ curves for each condition). (C) Effect of the isolation method and lyophilization on d_{10}, d_{50}, d_{90}, mean diameter, and mode of nanovesicles before and after lyophilization. Different letters indicate a significant difference ($p < 0.05$), while the same letter indicates no significant difference ($p > 0.05$). Two-way ANOVA, mean ± standard deviation, Tukey's multiple comparisons test; $n = 45$ total distribution curves generated for samples before and after lyophilization. (D) Protein and lipid content and number of particles per mL of nanovesicles at the end of the TFF process for batches produced using method A or B. t-test, mean ± standard

© 2026 The Author(s). Published by the Royal Society of Chemistry

with method A, indicating that, as expected, filtering on higher-dimension pores allows for isolating increased amounts of material; however, these differences were not statistically significant (Fig. 1D). This lack of significance is likely attributable to the high sample variability associated with the production process. In this initial phase, the concentration step was stopped when the final volume reached 25% of the initial volume, regardless of the protein or lipid concentration in the sample. Moving forward, the process will be optimized to standardize nanovesicle protein and lipid content by halting the concentration step upon reaching a target protein or lipid concentration, as previously described.[89] Nevertheless, method B allowed the isolation of a significantly higher number of nanovesicles (Fig. 1D) – an expected outcome, given that pre-filtration with a 1 μm pore size reduces the loss of proteins and nanovesicles compared to the 0.22 μm filter used in method A.

ATR-FTIR allowed visualization of the molecular fingerprint of nanovesicles. Both samples were enriched in lipids and proteins. Notably, the adsorption at the wavenumber 1610 cm^{-1}, characteristic of β-sheets and turns, indicated the presence of protein aggregates (Fig. 1E and S1). However, detailed analysis of adsorption band intensities (see Tables S3 and S4) demonstrated that nanovesicles obtained with method B have higher lipid content and an increased lipid-to-protein ratio. Moreover, broadening of the peaks in the 2850–2990 cm^{-1} region, typical of CH groups, indicates that nanovesicles isolated with method B contained a greater diversity of lipid and protein species compared to those prepared with method A. In particular, comparison of the maximum intensities of the IR adsorption peaks indicates that, following an additional ultracentrifugation step, the reduction in lipid concentration is twice as great in nanovesicles prepared using method A as in those prepared using method B. In contrast, the protein concentration decreases twofold more in nanovesicles prepared by method B, indicating that ultracentrifugation is more effective at removing proteins from the nanovesicles prepared with method B. Moreover, for nanovesicles prepared with both methods upon ultracentrifugation, the protein Amide I peak is shifted to lower wavenumbers (1610 cm^{-1}) in comparison to the typical values for α-helices (1640–1650 cm^{-1}), probably due to different protein conformation (aggregation or β-sheets). Upon ultracentrifugation of nanovesicles prepared with method B, most aggregated proteins were removed, and the peak at wavenumber 1648 cm^{-1} became more pronounced. This separation might not be as efficient for nanovesicles prepared with method A since the vesicles are smaller and closer in size to protein aggregates. Overall, FTIR analysis confirms that the isolated particles retain the spectral fingerprint expected for lipid bilayer vesicles while highlighting the contribution of co-isolated proteins associated with the nanovesicle surface. Considering the current limitations in the definition and purification of plant-derived EVs, the obtained samples can be more appropriately described as EV-enriched fractions. Therefore, the contribution of co-isolated biomolecules, including proteins and polysaccharides, to the observed physicochemical features cannot be completely excluded. Moreover, proteins and sugars are well known for their stabilizing effect on lipid membranes; as such, they may act together with mannitol, the cryoprotectant added, to prevent EV aggregation and fusion during lyophilization.[90]

To characterize and compare the nanoscale structural properties of the samples, SAXS measurements were performed (Fig. 1F). SAXS profiles of nanovesicles prepared with methods A and B exhibited a slope of approximately −2.7 at low q-vector values, indicating the presence of bidimensional objects (intact membrane vesicles) with an irregular surface, which indicates the presence of a diffusive protein corona of adsorbed biomolecules onto the membrane surface. The absence of sharp Bragg reflections further indicates that the vesicles preserve a fluid membrane organization rather than forming ordered lamellar aggregates. The SAXS curve of the nanovesicles prepared with method B displayed a steeper slope in the mid q-vector range (0.5–2 nm^{-1}), which indicates the presence, in the sample, of objects sized 10–13 nm, such as unfolded proteins, sugars, peptides in solution, or proteins associated with the membrane surface. Notably, the total X-ray scattering intensity for nanovesicles obtained with method A was approximately half that observed for method B, indicating a lower concentration of both nanovesicles and smaller objects in sample A (isolated using the 0.22 μm molecular cut-off filter), as expected.

3.2 *In vitro* biological characterization of apple-derived nanovesicles

The biological properties of freeze-dried nanovesicles obtained using methods A and B were evaluated by assessing their antioxidant, anti-elastase, and anti-tyrosinase activities. Only nanovesicles isolated using method B exhibited dose-dependent antioxidant activity (Fig. 2A). However, the maximum antioxidant activity, 25%, was observed only at the highest tested concentration (10 mg mL^{-1}). This outcome was expected and can be attributed to the different pore sizes of the filters used in the isolation process. Specifically, samples obtained using method A (0.22 μm cut-off filter) experienced a more significant exclusion of potentially active molecules, such as proteins, flavonoids, and pectin, compared to those obtained using method B (1 μm cut-off filter), which likely contributed to the reduced antioxidant capacity observed for method A. Similarly, only nanovesicles isolated using method B showed anti-tyrosinase activity, which reached 24.59% ±

deviation; $n = 3$ batches for each condition; *$p < 0.05$. (E) ATR-FTIR spectra of the samples obtained with method A or B and following further purification by ultracentrifugation (UC). (F) SAXS intensities as a function of the q-vector for nanovesicles obtained using method A (red triangles) and nanovesicles obtained using method B (black squares). The black lines are reported to guide the eye in detecting curve slopes over different q-range intervals.

© 2026 The Author(s). Published by the Royal Society of Chemistry

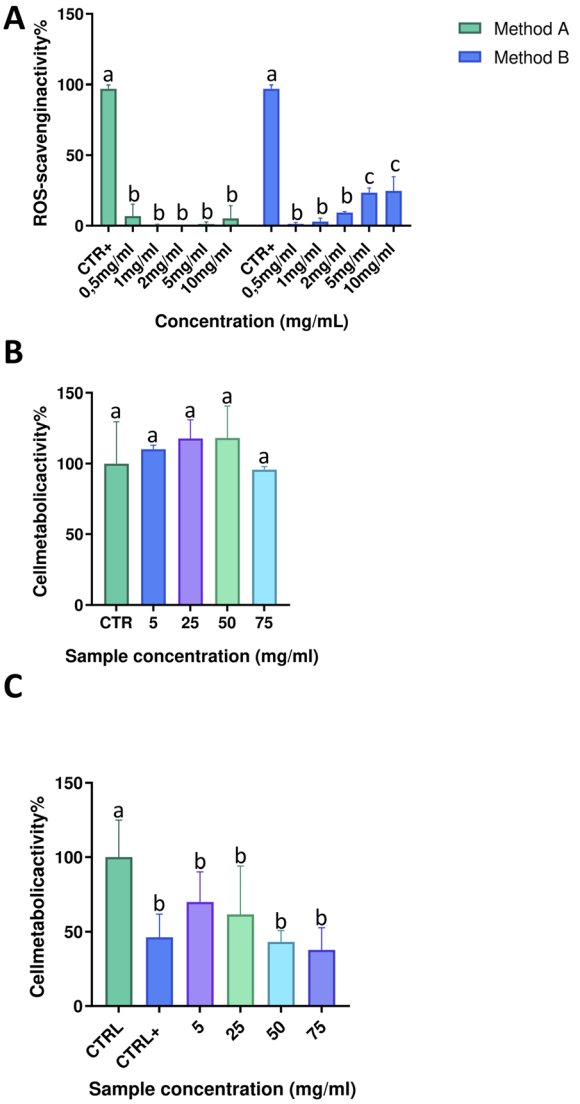


Fig. 2 (A) ROS-scavenging activity (%) of freeze-dried nanovesicles obtained using methods A and B and tested at increasing concentrations. Different letters indicate a significant difference between the means ($p < 0.05$), while the same letter indicates no significant difference between the means ($p > 0.05$). Two-way ANOVA, mean ± standard deviation, Tukey's multiple comparisons test; $n = 3$ for each concentration of each sample. (B) Cellular metabolic activity (%) of Caco-2 cells treated with different concentrations of nanovesicles isolated using method B and freeze-dried. The same letter indicates no significant difference between the means ($p > 0.05$). Two-way ANOVA, mean ± standard deviation; $n = 3$ for each concentration. (C) Protection from oxidative stress in Caco-2 cells treated with different concentrations of nanovesicles isolated using method B and freeze-dried. CTRL are cells untreated, while CTRL+ are cells treated with H_2O_2 but not with nanovesicles. Different letters indicate a significant difference between the means ($p < 0.05$), while the same letter indicates no significant difference between the means ($p > 0.05$). Two-way ANOVA, mean ± standard deviation, Tukey's multiple comparisons test; $n = 3$ for each concentration.

2.589 (mean value ± standard deviation, $n = 3$) at the highest concentration tested (10 mg mL^{-1}). In contrast, neither EV-enriched fraction exhibited anti-elastase activity under the conditions tested. These biological activities are likely influenced by the source material, including the type of fruit and the specific part utilized (*e.g.*, pulp, peel). This may explain why our findings differ from those previously reported in the literature, such as the antioxidant activity of EVs derived from tomato and grapefruit,[91] or the antityrosinase activity of EVs isolated from *Dendropanax morbifera*.[92] Importantly, in the present study, nanovesicles were isolated from dried apple press residue, which primarily consists of peel and seeds. Most of the EVs originating from the pulp are likely retained in the apple juice, which was not used as a source of nanovesicles in this work.

Regarding cytocompatibility, all tested samples were cytocompatible across all concentrations tested, as cellular metabolic activity did not differ significantly from that of the control, which was set at 100% (Fig. 2B). However, at none of the tested concentrations did the nanovesicles demonstrate the ability to protect the cells from oxidative stress induced by H_2O_2, as the metabolic activity of the treated cells did not differ significantly from that of the positive control (Fig. 2C).

3.3 Proteomic characterization of nanovesicles of *Malus domestica*

Characterization of the protein content of nanovesicles isolated using method B led to the identification of 673 proteins. To eliminate redundancy and obtain a refined list of unique protein entries, a pairwise global alignment algorithm was applied to the dataset. As a result, 588 non-redundant proteins were retained for further analysis (Tables S5 and S7). To generate a ranked list of the most abundant proteins, the average PSMs per protein were normalized based on their corresponding molecular weight (Table 1). Besides CRA1, a seed storage protein whose presence is consistent with nanovesicles primarily isolated from apple peel and seeds, the top ten most abundant proteins were mainly associated with metabolic pathways such as glycolysis and the oxidative pentose phosphate pathway. These included bifunctional enolase 2 (ENO2), glyceraldehyde-3-phosphate dehydrogenase (GAPC2), UTP-glucose-1-phosphate uridylyltransferase (UGP1), NADP-dependent malic enzyme 1 (NADP-ME1), 14-3-3-like protein (GRF3), and ATP synthase (T18C6.2). Furthermore, structural proteins such as actin (ACT7) and ubiquitin-ribosomal protein (RPS27AB), along with kinases, were also among the most abundant proteins identified.

In addition to glycolytic and carbohydrate metabolic processes, biosynthesis of secondary metabolites, and translation, a large proportion of proteins was linked to oxidative phosphorylation, particularly ATP synthase and ATPase subunits (Fig. 3), suggesting a potential role of nanovesicles in energy metabolism, as well as in membrane fusion and vesicular trafficking.[93] Furthermore, cytoskeleton-related proteins, such as tubulins and actins, together with several chaperones and heat shock proteins involved in protein folding and stress response, were enriched, supporting the role of apple-derived nanovesicles in structural integrity, stability, and mobility.

Beyond their value as compositional markers, several of the proteins identified in apple-derived nanovesicles may

© 2026 The Author(s). Published by the Royal Society of Chemistry

Table 1 List of 20 top-ranking proteins identified in nanovesicles of *Malus domestica* with corresponding homologous proteins in *Arabidopsis thaliana*. The normalized PSMs were obtained following the formula reported in Section 2.4.4

Accession uniprot *Malus domestica*	Gene name *Malus domestica*	Description	Accession uniprot *Arabidopsis thaliana*	Gene name *Arabidopsis thaliana*	Identity (%)	Bitscore	PSMs	Molecular weight (KDa)	nPSMs	Function
A0A498JXR5	DVH24_010597	Cupin type-1 domain-containing protein	P15455	CRA1	35.7	281.6	1104	67.1	1809.8	Seed storage protein
A0A498HKV6	DVH24_030694	Ubiquitin-like domain-containing protein	P59232	RPS27AB	96.8	238	67.5	17.7	419.5	Component of the 40S subunit of the ribosome; protein degradation *via* the proteasome
A0A498KJN5	DVH24_018017	Malic enzyme	O82191	NADP-ME1	81.9	944.5	239.5	64.6	407.8	Lipid metabolism
A0A498I3Y5	DVH24_039502	Actin	P53492	ACT7	98.7	755.4	120.5	41.7	317.9	Structural constituent of cytoskeleton
Q5UFR1	—	14-3-3 family protein	P42644	GRF3	90.9	445.3	58.5	29.7	216.7	Regulation of nutrient metabolism
A0A498HRI0	DVH24_033773	Glyceraldehyde-3-phosphate dehydrogenase	Q9FX54	GAPC2	92.5	624.4	61	39	172.1	Carbohydrate degradation; glycolysis
A0A498IHU7	DVH24_035008	Phosphopyruvate hydratase	P25696	ENO2	89.2	785	69.5	47.8	159.9	Carbohydrate degradation; glycolysis
J7MPY1	atp1	ATP synthase subunit α	F4IMB5	T18C6.2	93	905.2	68.5	55.3	136.3	Oxidative phosphorylation
A0A498J4G9	DVH24_035443	UTP-glucose-1-phosphate uridylyltransferase	P57751	UGP1	84.1	792.3	61	51.8	129.5	Carbohydrate metabolism
A0A498JUY7	DVH24_009939	Peptidyl-prolyl *cis*–trans isomerase	Q38900	CYP19-1	85.3	314.3	17.5	18.1	106.4	Protein folding
Q9M6R1	Hsp2	High molecular weight heat shock protein	Q9LHA8	HSP70-4	91.3	1156.7	68.5	71.2	105.8	Protein folding; protein ubiquitination
A0A498HFP0	DVH24_007552	Bet v I/Major latex protein domain-containing protein	Q96274	MLP2	42	125.9	16.5	17.8	102.0	Defense response
A0A223A9S9	rbcL	Ribulose bisphosphate carboxylase large chain	O03042	rbcL	94.5	941.4	45.5	52.6	95.2	Calvin's reductive pentose phosphate cycle; photosynthesys
A0A678V5H2	—	Xyloglucanase inhibitor-like protein	Q9ZVS5	F15K9.16	42.1	324.3	40.5	48.6	91.7	Proteolysis
A0A498KQC7	DVH24_033928	Annexin	Q9XEE2	ANN2	71	452.6	30	36.2	91.2	Secretion of Golgi-derived vesicles

© 2026 The Author(s). Published by the Royal Society of Chemistry

Table 1 (Contd.)

Accession uniprot *Malus domestica*	Gene name *Malus domestica*	Description	Accession uniprot *Arabidopsis thaliana*	Gene name *Arabidopsis thaliana*	Identity (%)	Bitscore	PSMs	Molecular weight (KDa)	nPSMs	Function
										during seedling development
A0A498I8L0	DVH24_040386	ATP synthase subunit β	Q9C5A9	T2K12.16	81.3	874.4	69	90.3	84.1	Proton-transporting ATP synthase activity
A0A498I8M1	DVH24_001855	Malate dehydrogenase	P93819	MDH1	90.4	597.8	26.5	35.5	82.1	Central metabolism and redox homeostasis
A0A498JN76	DVH24_007755	Tubulin α chain	P29511	TUBA6	96.7	891	36.5	49.5	81.1	Constituent of microtubules
A0A49816U2	DVH24_023505	Tubulin β chain	P29514	TUBB6	94.2	855.9	37	50.2	81.1	Constituent of microtubules
A0A498IWZ8	DVH24_021907	Phosphoglycerate kinase	Q9SAJ4	PGK3	90	708.4	31	42.3	80.6	Carbohydrate degradation; glycolysis

contribute to their interaction with biological membranes. In particular, the enrichment of ATP synthase/ATPase-related proteins, cytoskeletal components such as actins and tubulins, and membrane-associated chaperones is consistent with previous reports describing their involvement in vesicle organization, membrane remodeling, and vesicle trafficking. Although the functional role of these proteins in plant-derived EVs remains incompletely understood, their presence may contribute to the strong membrane affinity observed by SAXS and, more generally, to the physicochemical interaction of nanovesicles with biological interfaces. These findings suggest that the proteomic cargo of apple-derived nanovesicles may not only reflect their cellular origin but could also participate in determining their physicochemical behavior at biological interfaces, supporting their potential application as membrane-interacting nanocarriers.

3.4 Loading and membrane association of UA in apple-derived nanovesicles

Nanovesicles isolated using method B were selected as delivery carriers for UA. Nanovesicles were first dispersed in deionized water, and UA was subsequently associated with the nanovesicle-enriched fraction while keeping a constant EV lipid concentration and progressively reducing the UA concentration to achieve different UA : EV ratios (1 : 1, 1 : 2, 1 : 5, and 1 : 10). To facilitate UA loading and association with the nanovesicular fraction, samples were sonicated at 4 °C for 1 h. During this process, the shear forces can transiently perturb the lipid membrane and promote the partitioning of hydrophobic compounds into or onto vesicular lipid structures.[94–96]

As the UA amount decreases with respect to nanovesicles, a corresponding increase in UA loading efficiency was observed, while the amount of active ingredient adsorbed onto the dialysis membrane decreases (Table 2). Notably, due to its lipophilicity, UA tended to adsorb onto the membrane (which is also lipophilic) rather than concentrate in the dialysis water. Consequently, the concentration of UA detected in the aqueous phase remained below the LOQ. The operational encapsulation efficiency was 88.2%, 92.4%, 96.3%, and 94.0% at UA : EV ratios of 1 : 1, 1 : 2, 1 : 5, and 1 : 10, respectively. UA recovery ranged from 90.7% to 96.3% across all ratios, indicating limited losses during the loading procedure. Importantly, recovery of UA with the nanovesicle-enriched fraction does not establish its exclusive intravesicular localization, since strong association with the vesicular membrane or with other co-isolated components cannot be excluded.

Following UA encapsulation, the nanovesicles showed an increased particle size (Fig. 4A) and maintained their morphology (Fig. 4B).

FTIR spectra (Fig. 5A) showed that at a low UA concentration, the intensity of CH peaks at wavenumber 2850–2990 cm^{-1} decreased significantly, whereas the intensity of the Amide I and Amide II bands remained largely unaffected (Fig. S2, S3 and Tables S6, S7). The lipid-to-protein ratio, calculated from the relative peak areas (Table S8), decreased 1.7 times at low UA content, consistent with a partial displacement or

© 2026 The Author(s). Published by the Royal Society of Chemistry

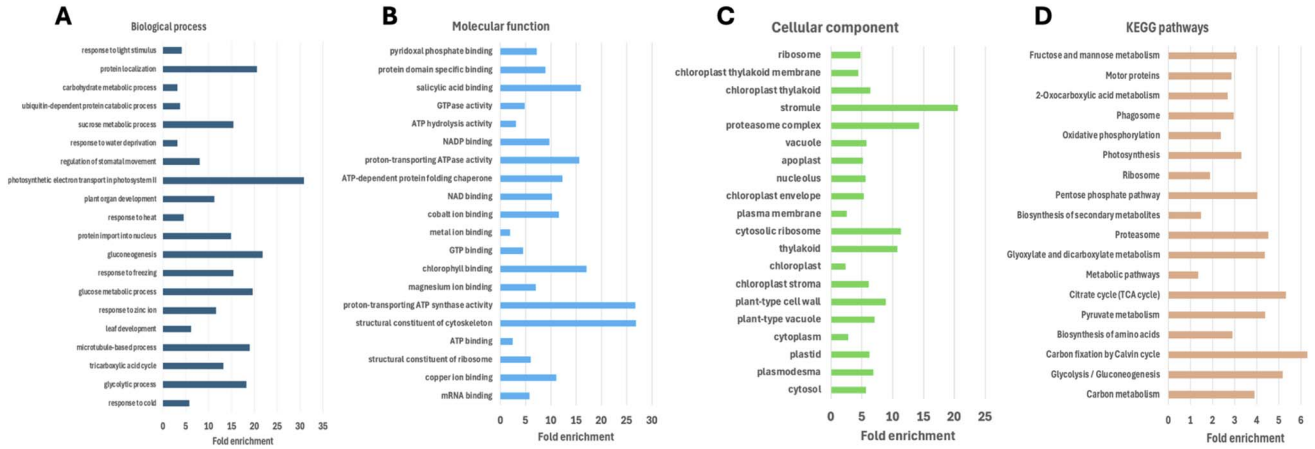


Fig. 3 (A) Biological processes, (B) molecular functions, (C) cellular components, (D) KEGG pathways enriched in the proteome characterized by analyzing nanovesicles obtained from apple, taking as reference the *Arabidopsis thaliana* database. Fold enrichment (FDR < 0.05) was calculated by means of the DAVID database.

Table 2 Loading, encapsulation efficiency, and overall recovery of UA in nanovesicles as a function of the UA : EV ratio. Data are reported as mean ± standard error, $n = 3$

UA : EV ratio	ppm of UA loaded into nanovesicles (μg g^{-1})	ppm of UA adsorbed onto the membrane (μg g^{-1})	Encapsulation efficiency (%)	Overall recovery (%)
1 : 1	2.89 ± 0.21	0.81 ± 0.02	88.24	90.70
1 : 2	1.51 ± 0.22	0.43 ± 0.01	92.44	95.04
1 : 5	0.68 ± 0.15	—	100	96.31
1 : 10	0.35 ± 0.06	—	100	93.96

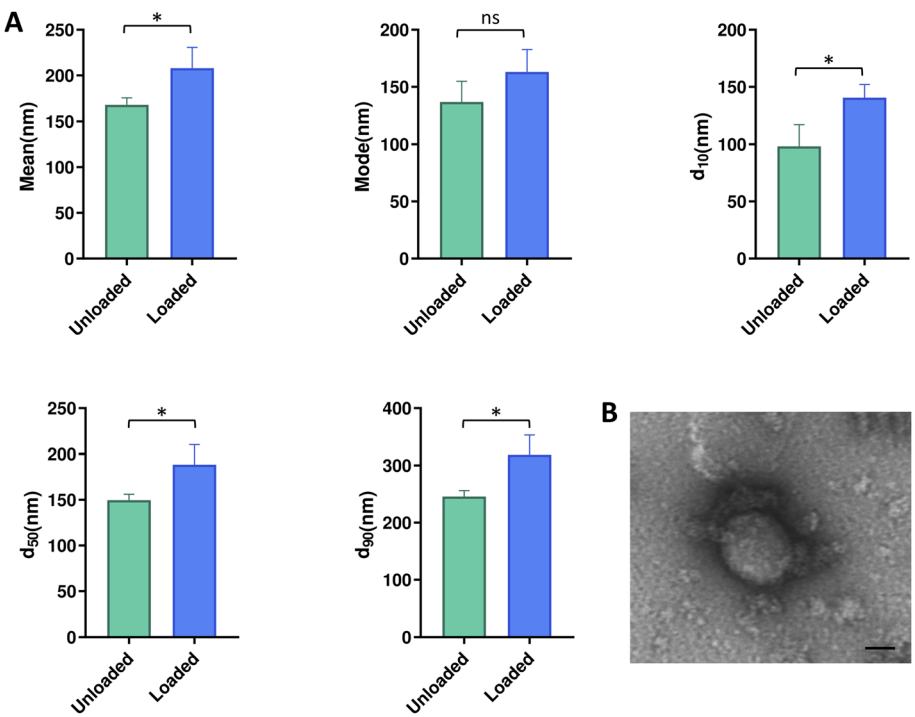


Fig. 4 (A) Effect of UA encapsulation on d_{10}, d_{50}, d_{90}, mean diameter, and mode of nanovesicles obtained with method B and freeze-dried. *$p < 0.05$; t-test, mean value ± standard deviation; $n = 15$ total distribution curves generated for samples. (B) Representative TEM image of UA-loaded nanovesicles. Scale bar: 50 nm.

© 2026 The Author(s). Published by the Royal Society of Chemistry

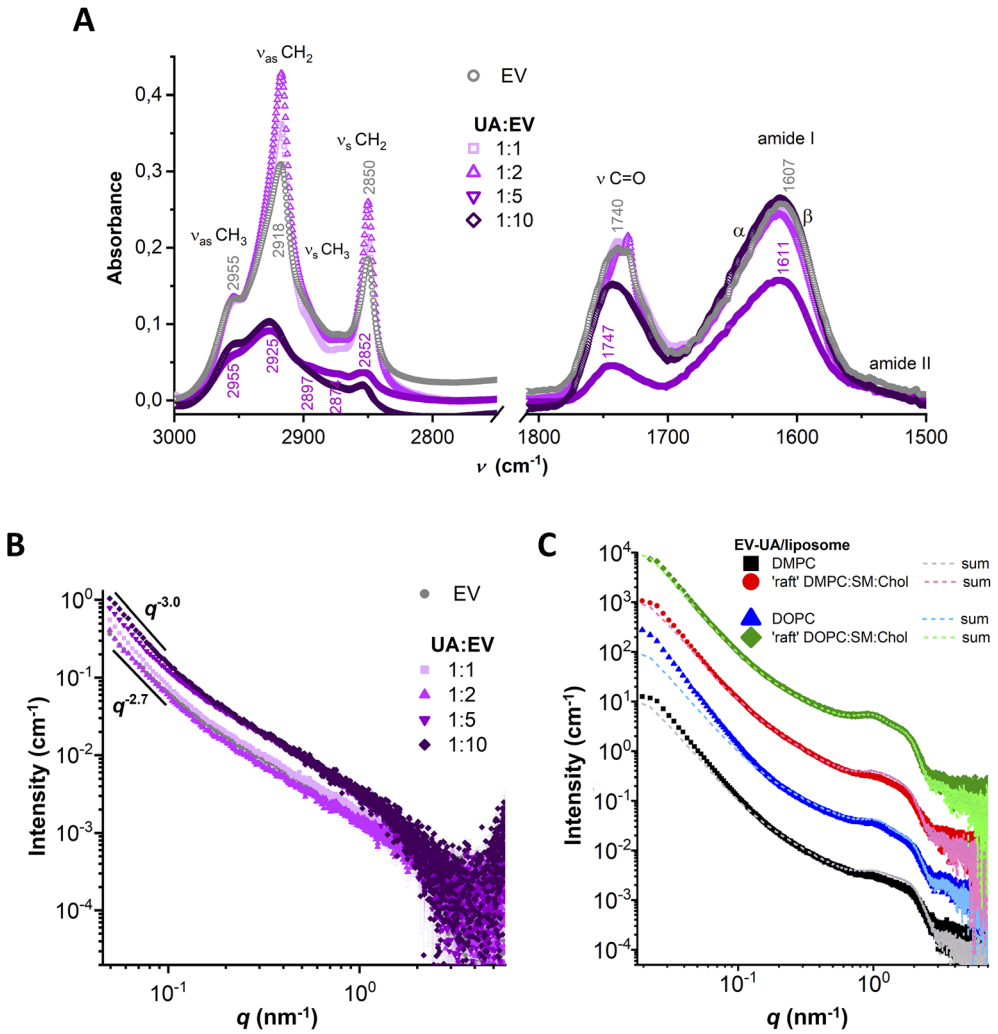


Fig. 5 (A) FTIR spectra of nanovesicles loaded with UA in different molar proportions in the wavenumber range of lipids (2990–2800 cm^{-1}) and proteins (1800–1500 cm^{-1}). (B) SAXS intensity curves for nanovesicles prepared with method B and loaded with UA in different ratios at 37 °C. (C) SAXS curves for nanovesicles loaded with UA (UA : EV ratio 1 : 5) mixed with liposomes composed of DMPC, DOPC, DMPC : Sphingomyelin : Cholesterol or DOPC : Sphingomyelin : Cholesterol (molar ratio 1 : 0.3 : 0.05) at 37 °C. The dashed lines correspond to the theoretical intensity of the mixture calculated as the arithmetic sum of scattering intensities of individual components. The SAXS curves were multiplied by successive factors of 100, 101, 102, and 103 (from bottom to top) for clarity.

reorganization of lipid chains caused by the association of UA with the lipid phase. At higher UA loading, no further spectral changes are observed, suggesting saturation of the available membrane-associated loading sites. Slightly higher ratios for loaded nanovesicles (1.4–1.5, see Table S8), compared to non-loaded nanovesicles (1.2), are probably caused by the overlapping of the C–H bands of lipids and excessive UA in the same range of wavenumbers.

SAXS curves (Fig. 5B) indicate a biphasic behavior of nanovesicles loaded with different UA concentrations. The forward X-ray scattering increases 1.5 times at a low concentration of added UA (UA : EV ratio 1 : 10 in Fig. 5B) in comparison to empty nanovesicles, indicating a significant increase in the size of the particles due to aggregation. However, at higher concentrations of UA, the forward scattering decreases almost to the same values as for non-loaded nanovesicles, which might be explained by the growth of aggregates formed by loaded nanovesicles and their eventual precipitation, and the scattering occurs from the remaining non-loaded nanovesicles. Moreover, the slope of the SAXS curves at low q increases from −2.7 to 3.0 at low concentrations of UA (see Fig. 5B and S4B), which confirms loose aggregate formation and could also indicate changes in membrane surface. The aggregation of nanovesicles was confirmed by measuring light scattering after sample separation with asymmetric flow field flow fractionation (Fig. S8), which demonstrated the two-fold increase in average gyration radius of nanovesicles after UA loading (from 70 to 150 nm at UA : EV ratio 1 : 5). At high q, the SAXS profile collected from nanovesicles loaded with low UA concentration has a sharper slope (Fig. 5B and S4C); a more pronounced form factor of the nanovesicle membrane is visible, due to the change in the contrast of the membrane layers for X-rays after UA insertion into the bilayer. At

© 2026 The Author(s). Published by the Royal Society of Chemistry

high concentrations of UA, the SAXS profile at high q becomes steeper and similar to that of non-loaded nanovesicles, allowing verification that only scattering from non-loaded nanovesicles is observed. These observations support a membrane-mediated loading mechanism in which UA strongly associates with the lipid component of the nanovesicle-enriched fraction while preserving the overall vesicular architecture. Therefore, the complementary SAXS and FTIR analyses consistently indicate strong UA–lipid interactions, although they do not resolve the precise localization of all recovered UA within the nanovesicle-enriched fraction.

To verify the affinity of nanovesicles with biological interfaces such as plasma membranes, the interaction between nanovesicles loaded with UA and synthetic lipid membranes in the form of LUVs in aqueous solution was investigated. Apple-derived nanovesicles demonstrated interaction with LUVs, consisting of either a single type of phospholipid (DMPC, DOPC) or a mixture of phospholipids with sphingomyelin and cholesterol (raft model DMPC : SM : Chol or DOPC : SM : Chol) (Fig. 5C). Such models allow for the examination of nanovesicle interaction with different domains of biomimetic membranes. Fig. 5C shows the scattering intensity profiles of the EV-UA/liposome mixtures in comparison with theoretical scattering calculated as the sum of scattering from EV-UA and liposomes. SAXS measurements showed that apple-derived nanovesicles do not destabilize biomimetic membranes, as the form factor of the lipid bilayer is preserved (broad peak at $q \approx 1\ nm^{-1}$, Fig. 5C and S6). However, slight changes in scattering intensity are observed at low q (<0.05 nm^{-1}) as well as in the range of membrane form factor scattering. In particular, the scattering at low q is higher than expected from two components and has steeper slopes for all types of membranes, indicating that aggregation in the mixture is promoted. On the other hand, the decrease in the intensity of the membrane form factor can be caused by the change of the membrane contrasts for X-rays due to an exchange of components such as lipids, proteins, or, most plausibly, UA between nanovesicles and liposomes. Indeed, the minima found at q 0.7 and 2.7 nm^{-1} are not affected upon interaction, implying that the thicknesses of biomimetic bilayers remain intact and therefore, if any exchange occurs, it is related to small molecules like UA. The observed variations in the scattering intensity of membrane form factors are more pronounced for the liposomes composed of DMPC only or DMPC : SM : Chol, possibly due to the lower fluidity of DMPC phospholipid with respect to DOPC. This finding suggests that UA has a higher affinity for less fluid lipids. At the same time, it was noticed that in both mixed systems with 'raft' models, DMPC : SM : Chol and DOPC : SM : Chol, the aggregation is reduced, possibly due to the higher LUV membrane rigidity and greater resistance to the rearrangements required to form compact aggregates.

3.5 Behavior of nanovesicle-associated UA at the intestinal epithelial interface

The behavior of free UA and UA associated with the apple-derived nanovesicle-enriched fraction at the intestinal epithelial interface was evaluated using Caco-2 cells. First, differentiated Caco-2 monolayers cultured in a Transwell® system were used to assess transepithelial transport in the apical-to-basolateral and basolateral-to-apical directions (Fig. 6). Free UA and nanovesicle-associated UA were administered at the same nominal initial UA concentration of 10 μg mL^{-1}. Because UA concentration was not analytically determined immediately after dosing, the first experimental measurement corresponded to 15 min.

At this first sampling time, the concentration of UA recovered from the donor medium was substantially higher for the nanovesicle-associated formulation than for free UA. Given the very low aqueous solubility of UA, this difference is consistent with the ability of the nanovesicle-enriched fraction to maintain a larger amount of UA in an analytically recoverable dispersed state.[49] Conversely, free UA may undergo rapid precipitation and/or adsorption following dilution into the experimental medium. However, in the absence of an analytical $t = 0$ measurement, the relative contribution of these processes

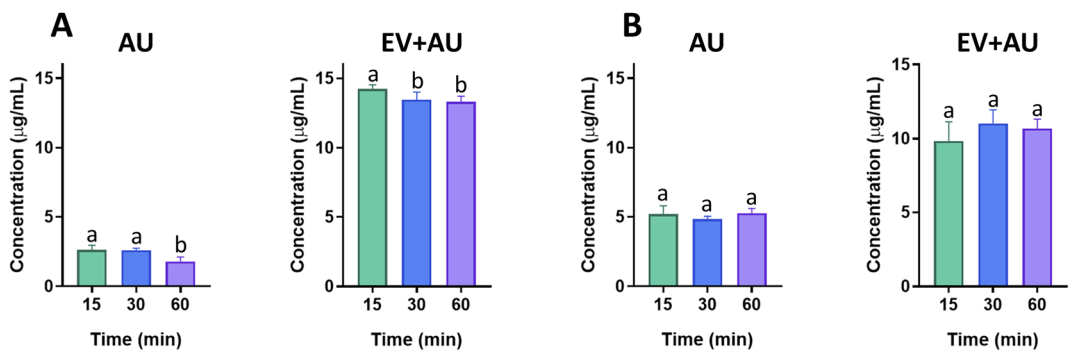


Fig. 6 Behavior of free and nanovesicle-associated UA at the Caco-2 epithelial interface. Residual UA concentrations in the donor compartment during apical-to-basolateral (A) and basolateral-to-apical (B) transport experiments across differentiated Caco-2 monolayers. Samples were administered at the same nominal UA concentration (10 μg mL^{-1}) and collected after 15, 30, and 60 min. UA remained below the analytical lower limit of quantification (LOQ; 0.015 μg mL^{-1}) in the receiver compartment at all investigated time points. Different letters indicate a significant difference between means ($p < 0.05$); same letters indicate no significant difference. Multifactor ANOVA, Least Significant Difference (LSD) multiple comparisons test; mean ± LSD, $n = 3$.

© 2026 The Author(s). Published by the Royal Society of Chemistry

Table 3 Distribution and mass balance of free and nanovesicle-associated UA following exposure to Caco-2 cells. Caco-2 cells were exposed to free UA or nanovesicle-associated UA at the same nominal dose of 10 μg per well for 30, 60, or 120 min. UA was independently quantified in the culture supernatant, PBS wash, and cell-associated fraction. Data are expressed as mean ± standard deviation of two independent wells ($n = 2$); each independent value was calculated from the mean of three technical LC–MS/MS determinations. UA amounts in the supernatant, PBS wash, and cell-associated fraction are reported as μg per well, while cell-associated UA was additionally normalized to the total number of recovered cells and expressed as μg UA per 10^6 cells. Total UA recovery was calculated as the sum of the quantified fractions and expressed both as μg per well and as a percentage of the nominally administered dose. The LOQ for UA was 0.015 μg mL^{-1} in the analyzed sample; values below the LOQ are reported as BLQ. For nanovesicle-associated UA, total recovery was calculated from the quantifiable supernatant and PBS fractions because cell-associated UA remained below the LOQ

Treatment	Time (min)	Supernatant UA (μg per well)	PBS wash UA (μg per well)	Cell-associated UA (μg per well)	Cell-associated UA (μg per 10^6 cells)	Total UA recovered (μg per well)	Recovery (%)
Nanovesicle-associated UA	30	8.757 ± 0.683	1.295 ± 1.164	BLQ	BLQ	10.052 ± 0.482	100.5 ± 4.8
Nanovesicle-associated UA	60	8.949 ± 0.208	1.189 ± 0.541	BLQ	BLQ	10.138 ± 0.333	101.4 ± 3.3
Nanovesicle-associated UA	120	9.681 ± 0.356	1.655 ± 0.607	BLQ	BLQ	11.336 ± 0.250	113.4 ± 2.5
Free UA	30	6.283 ± 0.521	0.701 ± 0.530	0.285 ± 0.156	0.1555 ± 0.0813	7.270 ± 0.166	72.7 ± 1.7
Free UA	60	5.786 ± 0.292	1.177 ± 0.159	0.762 ± 0.153	0.3490 ± 0.1490	7.725 ± 0.298	77.3 ± 3.0
Free UA	120	5.104 ± 0.079	1.332 ± 0.279	1.334 ± 0.123	0.8922 ± 0.2342	7.769 ± 0.481	77.7 ± 4.8

cannot be established, and the difference observed at 15 min should not be interpreted as evidence of differential epithelial uptake or retention. UA remained below the analytical LOQ (0.015 μg mL^{-1}) in the receiver compartment at all investigated time points and in both transport directions. Therefore, under the experimental conditions tested, neither free nor nanovesicle-associated UA showed detectable transepithelial transport. TEER values remained above 300 Ω cm^2 before and after the transport experiments, confirming preservation of monolayer barrier integrity throughout the experimental period.

A complementary Caco-2 cell-association experiment further clarified the fate of UA at the epithelial interface (Table 3). After normalization to cell number, free UA showed a clear time-dependent increase in the cell-associated fraction, from 0.1555 ± 0.0813 μg per 10^6 cells at 30 min to 0.3490 ± 0.1490 μg per 10^6 cells at 60 min and 0.8922 ± 0.2343 μg per 10^6 cells at 120 min. In contrast, cell-associated UA remained below the LOQ at all investigated time points following administration of nanovesicle-associated UA. This difference indicates that association with the nanovesicle-enriched fraction markedly limited the short-term association of UA with Caco-2 cells under the tested conditions. Consistent with this observation, a substantially greater amount of UA remained recoverable in the culture supernatant when administered with the nanovesicle-enriched fraction. Supernatant recovery ranged from 8.757 ± 0.683 to 9.681 ± 0.356 μg per well for nanovesicle-associated UA, compared with 6.283 ± 0.521 to 5.104 ± 0.079 μg per well for free UA over the 30–120 min exposure period. UA was also recovered in the PBS wash for both formulations, indicating that a fraction of the compound remained loosely associated with the cellular surface and/or well-associated material removed during washing. The overall mass balance further supported the different behavior of the two formulations. For nanovesicle-associated UA, the quantified recovery accounted for 100.5 ± 4.8%, 101.4 ± 3.3%, and 113.4 ± 2.5% of the nominally administered dose at 30, 60, and 120 min, respectively, with the great majority of UA remaining in the extracellular fractions. The recovery exceeding 100% at 120 min likely reflects analytical and sample-processing variability associated with the independent quantification of the different fractions and should therefore not be interpreted as an actual increase in UA amount. By contrast, total recovery of free UA remained lower, corresponding to 72.7 ± 1.7%, 77.3 ± 3.0%, and 77.7 ± 4.8% of the nominal dose at 30, 60, and 120 min, respectively. The incomplete recovery of free UA is consistent with its poor aqueous solubility and may reflect precipitation, adsorption to experimental surfaces, or other non-recovered fractions; however, the present experimental design does not allow these contributions to be distinguished quantitatively.

These findings support that under the conditions tested, nanovesicle association maintained UA predominantly in the extracellular, analytically recoverable fraction, while reducing its short-term association with Caco-2 cells and without producing detectable transepithelial transport. The limited cell association observed for nanovesicle-associated UA over the 30–120 min exposure period is not necessarily inconsistent with

© 2026 The Author(s). Published by the Royal Society of Chemistry

previous reports of plant-derived vesicle uptake by Caco-2 cells. Indeed, cellular internalization of plant-derived nanovesicles appears to be strongly time-dependent. Hossain *et al.* reported no detectable uptake of broccoli-derived nanovesicles after 2 h, whereas uptake became evident after prolonged exposure.[97] Similarly, *Citrus sinensis*-derived EVs showed limited intracellular localization in differentiated Caco-2 cells after 6 h, with substantially greater internalization after 24 h,[98] while uptake of garlic chive-derived vesicle-like nanoparticles increased progressively over 3–16 h.[99] These observations suggest that the relatively short exposure window investigated here may preferentially reflect the extracellular carrier behavior of the nanovesicle-enriched fraction rather than its longer-term interaction with intestinal epithelial cells. Importantly, the present experimental design quantifies UA recovered with the cellular fraction but does not distinguish surface-bound from internalized UA. Accordingly, the results are described in terms of cell-associated UA rather than cellular uptake. Likewise, no conclusions can be drawn regarding the cellular internalization of the nanovesicles themselves.

4. Conclusions

In this study, nanovesicle-enriched fractions were successfully isolated from dry apple press residues through a TFF-based manufacturing workflow followed by lyophilization. The process operated stably, supporting the feasibility of valorizing apple pomace through a scalable, membrane-based approach, although water consumption and downstream drying still require optimization. The resulting fractions displayed characteristic nanoscale morphology, retained their structural integrity after freeze-drying, showed favorable cytocompatibility, and had a complex protein and lipid composition. UA associated efficiently with the nanovesicle-enriched fraction, and SAXS and ATR-FTIR analyses revealed strong UA-lipid interactions accompanied by membrane reorganization. This association increased extracellular UA recovery compared with free UA, consistent with improved apparent dispersibility. It did not, however, enhance transepithelial transport and was associated with reduced short-term cell association of UA in Caco-2 cells.

Taken together, these results indicate that the nanovesicle-enriched fraction acts primarily as an extracellular stabilizing carrier, rather than as an enhancer of permeation or rapid cellular delivery, thereby supporting its potential to maintain poorly water-soluble bioactives in a dispersed and recoverable state at the intestinal epithelial interface.

Conflicts of interest

MLT is a co-founder and member of the company's advisory board PharmaExceed S.r.l. This company had no role in the design of the study, in the collection, analysis, or interpretation of data, in the writing of the manuscript, or in the decision to publish the results.

Data availability

Data will be made available upon reasonable request. The raw data from the ID02 beamline at ESRF are available at https://doi.esrf.fr/10.15151/ESRF-ES-1837447272 and https://doi.esrf.fr/10.15151/ESRF-ES-1925860640. Proteomic data are available from the ProteomeXchange Consortium repository at the site https://ftp://massive-ftp.ucsd.edu/v13/MSV000102353 (accessed on 03/07/2026).

Supplementary information (SI) is available. See DOI: https://doi.org/10.1039/d6fb00278a.

Acknowledgements

This work is part of the RESALE project, funded by the European Commission – NextGenerationEU and Compagnia di San Paolo. AM, GG and VR acknowledge the support of European Union – Next Generation EU Mission 4 Componente 1 (PRIN 2022 ID: 20223SM7T2 – Anastasia CUP: F53D23004980001, CUP G53D23003300001 and project EXTREME, CUP: G53D23007030001). This work benefited from access to the P12 beamline (EMBL Hamburg), an Instruct-ERIC center. Financial support was provided by Instruct-ERIC (PID: 37692). This work was further supported by the Department of Excellence 2023–2027 project "SCALE UP", funded by the Italian Ministry of University and Research, Department of Molecular Biotechnology and Translational Medicine of the University of Milan. The authors acknowledge the European Synchrotron Radiation Facility for the provision of synchrotron radiation facilities under proposal numbers SC-5603 and LS-3423. They would also like to thank Dr Gouranga Manna and Dr Austin Hubley for assistance and support in using beamline ID02. The authors also acknowledge the Partnership for Soft-Condensed Matter laboratories in Grenoble for the use of the laboratories and instrumentation, and Pierre Lloria for his assistance. The synchrotron SAXS data were also collected at beamline P12 operated by EMBL Hamburg at the PETRA III storage ring (DESY Hamburg, Germany) within the proposal SAXS-1436. The authors would like to thank Dr Clement Blanchet from EMBL for the assistance in using the P12 beamline and Dr Baohu Wu from Jülich Center for Neutron Science at Heinz Maier-Leibnitz Zentrum, Forschungszentrum Jülich, for the preliminary SAXS measurements. Finally, the authors also thank Prof Federica Pollastro from the Department of Pharmaceutical Sciences, University of Piemonte Orientale, for providing the ursolic acid.

References

1 M. Tkach and C. Théry, Communication by Extracellular Vesicles: Where We Are and Where We Need to Go, *Cell*, 2016, **164**, 1226–1232, DOI: 10.1016/j.cell.2016.01.043.

2 A. Dixson, T. Dawson, D. Di Vizio and A. Weaver, Context-specific regulation of extracellular vesicle biogenesis and cargo selection, *Nat. Rev. Mol. Cell Biol.*, 2023, **24**, 454–476, DOI: 10.1038/s41580-023-00576-0.

3 M. Yanez-Mo, P. R. M. Siljander, Z. Andreu, A. B. Zavec, F. E. Borras, E. I. Buzas, K. Buzas, E. Casal, F. Cappello,

© 2026 The Author(s). Published by the Royal Society of Chemistry

J. Carvalho, *et al.*, Biological properties of extracellular vesicles and their physiological functions, *J. Extracell. Vesicles*, 2015, **14**(4), 27066, DOI: 10.3402/jev.v4.27066.

4 A. Ambrosone, A. Barbulova, E. Cappetta, F. Cillo, M. De Palma, M. Ruocco and G. Pocsfalvi, Plant Extracellular Vesicles: Current Landscape and Future Directions, *Plants*, 2023, **12**(24), 4141, DOI: 10.3390/plants12244141.

5 Y. Wang, J. Wang, J. Ma, Y. Zhou and R. Lu, Focusing on Future Applications and Current Challenges of Plant Derived Extracellular Vesicles, *Pharmaceuticals*, 2022, **15**(6), 708, DOI: 10.3390/ph15060708.

6 K. Wang, Q. Chen, Y. Shao, S. Yin, C. Liu, Y. Liu, R. Wang, T. Wang, Y. Qiu and H. Yu, Anticancer activities of TCM and their active components against tumor metastasis, *Biomed. Pharmacother.*, 2021, **133**, 111044, DOI: 10.1016/j.biopha.2020.111044.

7 M. Trentini, I. Zanolla, F. Zanotti, E. Tiengo, D. Licastro, S. Dal Monego, L. Lovatti and B. Zavan, Apple Derived Exosomes Improve Collagen Type I Production and Decrease MMPs during Aging of the Skin through Downregulation of the NF-κB Pathway as Mode of Action, *Cells*, 2022, **11**(24), 3950, DOI: 10.3390/cells11243950.

8 X. Zhao, F. Yin, L. Fu, Y. Ma, L. Ye, Y. Huang, W. Fan, W. Gao, Y. Cai and X. Mou, Garlic-derived exosome-like nanovesicles as a hepatoprotective agent alleviating acute liver failure by inhibiting CCR2/CCR5 signaling and inflammation, *Biomater. Adv.*, 2023, **154**, 213592, DOI: 10.1016/j.bioadv.2023.213592.

9 B. Liu, Y. Lu, X. Chen, P. Muthuraj, X. Li, M. Pattabiraman, J. Zempleni, S. Kachman, S. Natarajan and J. Yu, Protective Role of Shiitake Mushroom-Derived Exosome-Like Nanoparticles in D-Galactosamine and Lipopolysaccharide-Induced Acute Liver Injury inMice, *Nutrients*, 2020, **12**(2), 477, DOI: 10.3390/nu12020477.

10 X. Zhang, Z. Pan, Y. Wang, P. Liu and K. Hu, Taraxacum officinale-derived exosome-like nanovesicles modulate gut metabolites to prevent intermittent hypoxia-induced hypertension, *Biomed. Pharmacother.*, 2023, **161**, 114572, DOI: 10.1016/j.biopha.2023.114572.

11 K. Sundaram, J. Mu, A. Kumar, J. Behera, C. Lei, M. Sriwastva, F. Xu, G. Dryden, L. Zhang, S. Chen, *et al.*, Garlic exosome-like nanoparticles reverse high-fat diet induced obesity via the gut/brain axis, *Theranostics*, 2022, **12**, 1220–1246, DOI: 10.7150/thno.65427.

12 Y. Lee, D. Jeong, Y. Jeun, H. Choe and S. Yang, Preventive and ameliorative effects of potato exosomes on UVB-induced photodamage in keratinocyte HaCaT cells, *Mol. Med. Rep.*, 2023, **28**(3), 167, DOI: 10.3892/mmr.2023.13054.

13 F. Xu, J. Mu, Y. Teng, X. Zhang, K. Sundaram, M. Sriwastva, A. Kumar, C. Lei, L. Zhang, Q. Liu, *et al.*, Restoring Oat Nanoparticles Mediated Brain Memory Function of Mice Fed Alcohol by Sorting Inflammatory Dectin-1 Complex Into Microglial Exosomes, *Small*, 2022, **18**(6), 2105385, DOI: 10.1002/smll.202105385.

14 R. Huang, B. Jia, D. Su, M. Li, Z. Xu, C. He, Y. Huang, H. Fan, H. Chen and F. Cheng, Plant exosomes fused with engineered mesenchymal stem cell-derived nanovesicles for synergistic therapy of autoimmune skin disorders, *J. Extracell. Vesicles*, 2023, **12**(10), e12361, DOI: 10.1002/jev2.12361.

15 F. Wang, M. Yuan, C. Shao, N. Ji, H. Zhang and C. Li, Momordica charantia-Derived Extracellular Vesicles Provide Antioxidant Protection in Ulcerative Colitis, *Molecules*, 2023, **28**(17), 6182, DOI: 10.3390/molecules28176182.

16 E. Berger, P. Colosetti, A. Jalabert, E. Meugnier, O. Wiklander, J. Jouhet, E. Errazurig-Cerda, S. Chanon, D. Gupta, G. Rautureau, *et al.*, Use of Nanovesicles from Orange Juice to Reverse Diet-Induced Gut Modifications in Diet-Induced Obese Mice, *Mol. Ther.–Methods Clin. Dev.*, 2020, **18**, 880–892, DOI: 10.1016/j.omtm.2020.08.009.

17 S. Li, R. Zhang, A. Wang, Y. Li, M. Zhang, J. Kim, Y. Zhu, Q. Wang, Y. Zhang, Y. Wei, *et al.*, Panax notoginseng: derived exosome-like nanoparticles attenuate ischemia reperfusion injury via altering microglia polarization, *J. Nanobiotechnol.*, 2023, **21**(1), 416, DOI: 10.1186/s12951-023-02161-1.

18 M. Zhang, E. Viennois, M. Prasad, Y. Zhang, L. Wang, Z. Zhang, M. Han, B. Xiao, C. Xu, S. Srinivasan, *et al.*, Edible ginger-derived nanoparticles: A novel therapeutic approach for the prevention and treatment of inflammatory bowel disease and colitis-associated cancer, *Biomaterials*, 2016, **101**, 321–340, DOI: 10.1016/j.biomaterials.2016.06.018.

19 Y. Lu, J. Xu, R. Tang, P. Zeng, Z. Li, J. You, T. Li, T. Zhang, X. Ma, Y. He, *et al.*, Edible pueraria lobata-derived exosome-like nanovesicles ameliorate dextran sulfate sodium-induced colitis associated lung inflammation through modulating macrophage polarization, *Biomed. Pharmacother.*, 2024, **170**, 116098, DOI: 10.1016/j.biopha.2023.116098.

20 M. Zhu, H. Xu, Y. Liang, J. Xu, N. Yue, Y. Zhang, C. Tian, J. Yao, L. Wang, Y. Nie, *et al.*, Edible exosome-like nanoparticles from portulaca oleracea L mitigate DSS-induced colitis via facilitating double-positive CD4+CD8+T cells expansion, *J. Nanobiotechnol.*, 2023, **21**(1), 309, DOI: 10.1186/s12951-023-02065-0.

21 S. Ju, J. Mu, T. Dokland, X. Zhuang, Q. Wang, H. Jiang, X. Xiang, Z. Deng, B. Wang, L. Zhang, *et al.*, Grape Exosome-like Nanoparticles Induce Intestinal Stem Cells and Protect Mice From DSS-Induced Colitis, *Mol. Ther.*, 2013, **21**, 1345–1357, DOI: 10.1038/mt.2013.64.

22 M. Cao, H. Yan, X. Han, L. Weng, Q. Wei, X. Sun, W. Lu, Q. Wei, J. Ye, X. Cai, *et al.*, Ginseng-derived nanoparticles alter macrophage polarization to inhibit melanoma growth, *J. Immunother. Cancer*, 2019, **7**(1), 326, DOI: 10.1186/s40425-019-0817-4.

23 J. Kim, Y. Zhu, S. Chen, D. Wang, S. Zhang, J. Xia, S. Li, Q. Qiu, H. Lee and J. Wang, Anti-glioma effect of ginseng-derived exosomes-like nanoparticles by active blood-brain-barrier penetration and tumor microenvironment modulation, *J. Nanobiotechnol.*, 2023, **21**(1), 253, DOI: 10.1186/s12951-023-02006-x.

 © 2026 The Author(s). Published by the Royal Society of Chemistry

24 R. Anusha, M. Ashin and S. Priya, Ginger exosome-like nanoparticles (GELNs) induced apoptosis, cell cycle arrest, and anti-metastatic effects in triple-negative breast cancer MDA-MB-231 cells, *Food Chem. Toxicol.*, 2023, **182**, 114102, DOI: 10.1016/j.fct.2023.114102.

25 Q. Chen, M. Zu, H. Gong, Y. Ma, J. Sun, S. Ran, X. Shi, J. Zhang and B. Xiao, Tea leaf-derived exosome-like nanotherapeutics retard breast tumor growth by pro-apoptosis and microbiota modulation, *J. Nanobiotechnol.*, 2023, **21**(1), 6, DOI: 10.1186/s12951-022-01755-5.

26 Q. Chen, Q. Li, Y. Liang, M. Zu, N. Chen, B. Canup, L. Luo, C. Wang, L. Zeng and B. Xiao, Natural exosome-like nanovesicles from edible tea flowers suppress metastatic breast cancer via ROS generation and microbiota modulation, *Acta Pharm. Sin. B*, 2022, **12**, 907–923, DOI: 10.1016/j.apsb.2021.08.016.

27 M. Yang, X. Liu, Q. Luo, L. Xu and F. Chen, An efficient method to isolate lemon derived extracellular vesicles for gastric cancer therapy, *J. Nanobiotechnol.*, 2020, **18**(1), 100, DOI: 10.1186/s12951-020-00656-9.

28 D. Sasaki, K. Kusamori, Y. Takayama, S. Itakura, H. Todo and M. Nishikawa, Development of nanoparticles derived from corn as mass producible bionanoparticles with anticancer activity, *Sci. Rep.*, 2021, **11**, 22818, DOI: 10.1038/s41598-021-02241-y.

29 X. Han, Q. Wei, Y. Lv, L. Weng, H. Huang, Q. Wei, M. Li, Y. Mao, D. Hua, X. Cai, *et al.*, Ginseng-derived nanoparticles potentiate immune checkpoint antibody efficacy by reprogramming the cold tumor microenvironment, *Mol. Ther.*, 2022, **30**, 327–340, DOI: 10.1016/j.ymthe.2021.08.028.

30 Y. Lv, M. Li, L. Weng, H. Huang, Y. Mao, D. Yang, Q. Wei, M. Zhao, Q. Wei, K. Rui, *et al.*, Ginseng-derived nanoparticles reprogram macrophages to regulate arginase-1 release for ameliorating T cell exhaustion in tumor microenvironment, *J. Exp. Clin. Cancer Res.*, 2023, **42**(1), 322, DOI: 10.1186/s13046-023-02888-7.

31 G. Castelli, M. Logozzi, D. Mizzoni, R. Di Raimo, A. Cerio, V. Dolo, L. Pasquini, M. Screnci, T. Ottone, U. Testa, *et al.*, Ex Vivo Anti-Leukemic Effect of Exosome-like Grapefruit-Derived Nanovesicles from Organic Farming-The Potential Role of Ascorbic Acid, *Int. J. Mol. Sci.*, 2023, **24**(21), 15663, DOI: 10.3390/ijms242115663.

32 T. Chen, B. Ma, S. Lu, L. Zeng, H. Wang, W. Shi, L. Zhou, Y. Xia, X. Zhang, J. Zhang, *et al.*, Cucumber-Derived Nanovesicles Containing Cucurbitacin B for Non-Small Cell Lung Cancer Therapy, *Int. J. Nanomed.*, 2022, **17**, 3583–3599, DOI: 10.2147/IJN.S362244.

33 H. Takakura, T. Nakao, T. Narita, M. Horinaka, Y. Nakao-Ise, T. Yamamoto, Y. Iizumi, M. Watanabe, Y. Sowa, K. Oda, *et al.*, Citrus limon L.-Derived Nanovesicles Show an Inhibitory Effect on Cell Growth in p53-Inactivated Colorectal Cancer Cells via the Macropinocytosis Pathway, *Biomedicines*, 2022, **10**(6), 1352, DOI: 10.3390/biomedicines10061352.

34 Q. Gao, N. Chen, B. Li, M. Zu, Y. Ma, H. Xu, Z. Zhu, R. Reis, S. Kundu and B. Xiao, Natural lipid nanoparticles extracted from Morus nigra L. leaves for targeted treatment of hepatocellular carcinoma via the oral route, *J. Nanobiotechnol.*, 2024, **22**(1), 4, DOI: 10.1186/s12951-023-02286-3.

35 M. Potestà, V. Roglia, M. Fanelli, E. Pietrobono, A. Gismondi, S. Vumbaca, R. Tsangueu, A. Canini, V. Colizzi, S. Grelli, *et al.*, Effect of microvesicles from Moringa oleifera containing miRNA on proliferation and apoptosis in tumor cell lines, *Cell Death Discovery*, 2020, **6**, 43, DOI: 10.1038/s41420-020-0271-6.

36 L. Yang, W. Jin, X. Tang, S. Zhang, R. Ma, D. Zhao and L. Sun, Ginseng-derived nanoparticles inhibit lung cancer cell epithelial mesenchymal transition by repressing pentose phosphate pathway activity, *Front. Oncol.*, 2022, **12**, 942020, DOI: 10.3389/fonc.2022.942020.

37 Y. Teng, Y. Ren, M. Sayed, X. Hu, C. Lei, A. Kumar, E. Hutchins, J. Mu, Z. Deng, C. Luo, *et al.*, Plant-Derived Exosomal MicroRNAs Shape the Gut Microbiota, *Cell Host Microbe*, 2018, **24**, 637, DOI: 10.1016/j.chom.2018.10.001.

38 X. Wang, Y. Liu, X. Dong, T. Duan, C. Wang, L. Wang, X. Yang, H. Tian and T. Li, peu-MIR2916-p3-enriched garlic exosomes ameliorate murine colitis by reshaping gut microbiota, especially by boosting the anti-colitic Bacteroides thetaiotaomicron, *Pharmacol. Res.*, 2024, **200**, 107071, DOI: 10.1016/j.phrs.2024.107071.

39 W. Zhan, M. Deng, X. Huang, D. Xie, X. Gao, J. Chen, Z. Shi, J. Lu, H. Lin and P. Li, Pueraria lobata-derived exosome-like nanovesicles alleviate osteoporosis by enhacning autophagy, *J. Controlled Release*, 2023, **364**, 644–653, DOI: 10.1016/j.jconrel.2023.11.020.

40 F. Qiu, J. Wang, M. Guo, X. Li, C. Shi, F. Wu, H. Zhang, H. Ying and C. Yu, Rgl-exomiR-7972, a novel plant exosomal microRNA derived from fresh Rehmanniae Radix, ameliorated lipopolysaccharide-induced acute lung injury and gut dysbiosis, *Biomed. Pharmacother.*, 2023, **165**, 115007, DOI: 10.1016/j.biopha.2023.115007.

41 Z. Zhu, L. Liao, M. Gao and Q. Liu, Garlic-derived exosome-like nanovesicles alleviate dextran sulphate sodium-induced mouse colitis via the TLR4/MyD88/NF-κB pathway and gut microbiota modulation, *Food Funct.*, 2023, **14**, 7520–7534, DOI: 10.1039/d3fo01094e.

42 C. Lei, Y. Teng, L. He, M. Sayed, J. Mu, F. Xu, X. Zhang, A. Kumar, K. Sundaram, M. Sriwastva, *et al.*, Lemon exosome-like nanoparticles enhance stress survival of gut bacteria by RNase P-mediated specific tRNA decay, *iScience*, 2021, **24**(6), 102511, DOI: 10.1016/j.isci.2021.102511.

43 C. Lei, J. Mu, Y. Teng, L. He, F. Xu, X. Zhang, K. Sundaram, A. Kumar, M. Sriwastva, M. Lawrenz, *et al.*, Lemon Exosome-like Nanoparticles-Manipulated Probiotics Protect Mice from C. diff Infection, *iScience*, 2020, **23**(10), 101571, DOI: 10.1016/j.isci.2020.101571.

44 W. Qiang, J. Li, R. Ruan, Q. Li, X. Zhang, A. Yan and H. Zhu, Plant-derived extracellular vesicles as a promising anti-tumor approach: A comprehensive assessment of effectiveness, safety, and mechanisms, *Phytomedicine*, 2024, **130**, 155750, DOI: 10.1016/j.phymed.2024.155750.

© 2026 The Author(s). Published by the Royal Society of Chemistry

45 B. Zhao, H. Lin, X. Jiang, W. Li, Y. Gao, M. Li, Y. Yu, N. Chen and J. Gao, Exosome-like nanoparticles derived from fruits, vegetables, and herbs: innovative strategies of therapeutic and drug delivery, *Theranostics*, 2024, **14**, 4598–4621, DOI: 10.7150/thno.97096.

46 A. Vargason, A. Anselmo and S. Mitragotri, The evolution of commercial drug delivery technologies, *Nat. Biomed. Eng.*, 2021, **5**, 951–967, DOI: 10.1038/s41551-021-00698-w.

47 P. Akuma, O. Okagu and C. Udenigwe, Naturally Occurring Exosome Vesicles as Potential Delivery Vehicle for Bioactive Compounds, *Front. Sustain. Food Syst.*, 2019, **3**, 23, DOI: 10.3389/fsufs.2019.00023.

48 X. Wang, C. Xin, Y. Zhou and T. Sun, Plant-Derived Vesicle-like Nanoparticles: The Next-Generation Drug Delivery Nanoplatforms, *Pharmaceutics*, 2024, **16**(5), 588, DOI: 10.3390/pharmaceutics16050588.

49 Z. Erana-Perez, M. Igartua, E. Santos-Vizcaino and R. Hernandez, Genetically engineered loaded extracellular vesicles for drug delivery, *Trends Pharmacol. Sci.*, 2024, **45**, 350–365, DOI: 10.1016/j.tips.2024.02.006.

50 Z. Fang and K. Liu, Plant-derived extracellular vesicles as oral drug delivery carriers, *J. Controlled Release*, 2022, **350**, 389–400, DOI: 10.1016/j.jconrel.2022.08.046.

51 M. Langellotto, G. Rassu, C. Serri, S. Demartis, P. Giunchedi and E. Gavini, Plant-derived extracellular vesicles: a synergetic combination of a drug delivery system and a source of natural bioactive compounds, *Drug Delivery Transl. Res.*, 2025, **15**, 831–845, DOI: 10.1007/s13346-024-01698-4.

52 Y. Zhao, H. Tan, J. Zhang, B. Pan, N. Wang, T. Chen, Y. Shi and Z. Wang, Plant-Derived Vesicles: A New Era for Anti-Cancer Drug Delivery and Cancer Treatment, *Int. J. Nanomed.*, 2023, **18**, 6847–6868, DOI: 10.2147/IJN.S432279.

53 E. Calzoni, A. Bertoldi, G. Cusumano, S. Buratta, L. Urbanelli and C. Emiliani, Plant-Derived Extracellular Vesicles: Natural Nanocarriers for Biotechnological Drugs, *Processes*, 2024, **12**(12), 2938, DOI: 10.3390/pr12122938.

54 M. Lian, W. Chng, J. Liang, H. Yeo, C. Lee, M. Belaid, M. Tollemeto, M. Wacker, B. Czarny and G. Pastorin, Plant-derived extracellular vesicles: Recent advancements and current challenges on their use for biomedical applications, *J. Extracell. Vesicles*, 2022, **11**(12), e12283, DOI: 10.1002/jev2.12283.

55 J. You, S. Kang and W. Rhee, Isolation of cabbage exosome-like nanovesicles and investigation of their biological activities in human cells, *Bioact. Mater.*, 2021, **6**, 4321–4332, DOI: 10.1016/j.bioactmat.2021.04.023.

56 M. Zhang, B. Xiao, H. Wang, M. Han, Z. Zhang, E. Viennois, C. Xu and D. Merlin, Edible Ginger-derived Nano-lipids Loaded with Doxorubicin as a Novel Drug-delivery Approach for Colon Cancer Therapy, *Mol. Ther.*, 2016, **24**, 1783–1796, DOI: 10.1038/mt.2016.159.

57 W. Niu, Q. Xiao, X. Wang, J. Zhu, J. Li, X. Liang, Y. Peng, C. Wu, R. Lu, Y. Pan, *et al.*, A Biomimetic Drug Delivery System by Integrating Grapefruit Extracellular Vesicles and Doxorubicin-Loaded Heparin-Based Nanoparticles for Glioma Therapy, *Nano Lett.*, 2021, **21**, 1484–1492, DOI: 10.1021/acs.nanolett.0c04753.

58 Q. Wang, X. Zhuang, J. Mu, Z. Deng, H. Jiang, X. Xiang, B. Wang, J. Yan, D. Miller and H. Zhang, Delivery of therapeutic agents by nanoparticles made of grapefruit-derived lipids, *Nat. Commun.*, 2013, **4**, 1867, DOI: 10.1038/ncomms2886.

59 M. Pomatto, C. Gai, F. Negro, L. Massari, M. Deregibus, C. Grange, F. De Rosa and G. Camussi, Plant-Derived Extracellular Vesicles as a Delivery Platform for RNA-Based Vaccine: Feasibility Study of an Oral and Intranasal SARS-CoV-2 Vaccine, *Pharmaceutics*, 2023, **15**(3), 974, DOI: 10.3390/pharmaceutics15030974.

60 X. Zhuang, Y. Teng, A. Samykutty, J. Mu, Z. Deng, L. Zhang, P. Cao, Y. Rong, J. Yan, D. Miller, *et al.*, Grapefruit-derived Nanovectors Delivering Therapeutic miR17 Through an Intranasal Route Inhibit Brain Tumor Progression, *Mol. Ther.*, 2016, **24**, 96–105, DOI: 10.1038/mt.2015.188.

61 Y. Teng, J. Mu, X. Hu, A. Samykutty, X. Zhuang, Z. Deng, L. Zhang, P. Cao, J. Yan, D. Miller, *et al.*, Grapefruit-derived nanovectors deliver miR-18a for treatment of liver metastasis of colon cancer by induction of M1 macrophages, *OncoTargets*, 2016, **7**, 25683–25697, DOI: 10.18632/oncotarget.8361.

62 M. Zhang, X. Wang, M. Han, J. Collins and D. Merlin, Oral administration of ginger-derived nanolipids loaded with siRNA as a novel approach for efficient siRNA drug delivery to treat ulcerative colitis, *Nanomedicine*, 2017, **12**, 1927–1943, DOI: 10.2217/nnm-2017-0196.

63 Z. Li, H. Wang, H. Yin, C. Bennett, H. Zhang and P. Guo, Arrowtail RNA for Ligand Display on Ginger Exosome-like Nanovesicles to Systemic Deliver siRNA for Cancer Suppression, *Sci. Rep.*, 2018, **8**, 14644, DOI: 10.1038/s41598-018-32953-7.

64 X. Wang, M. Zhang, S. Flores, R. Woloshun, C. Yang, L. Yin, P. Xiang, X. Xu, M. Garrick, S. Vidyasagar, *et al.*, Oral Gavage of Ginger Nanoparticle-Derived Lipid Vectors Carrying Dmt1 siRNA Blunts Iron Loading in Murine Hereditary Hemochromatosis, *Mol. Ther.*, 2019, **27**, 493–506, DOI: 10.1016/j.ymthe.2019.01.003.

65 S. Lee, Y. Kim, S. Chung and S. Park, Recent Studies On Ursolic Acid And Its Biological And Pharmacological Activity, *EXCLI J.*, 2016, **15**, 221–228.

66 M. Zhao, F. Wu, Z. Tang, X. Yang, Y. Liu, F. Wang and B. Chen, Anti-inflammatory and antioxidant activity of ursolic acid: a systematic review and meta-analysis, *Front. Pharmacol.*, 2023, **14**, 1256946, DOI: 10.3389/fphar.2023.1256946.

67 A. Kornel, M. Nadile, M. Retsidou, M. Sakellakis, K. Gioti, A. Beloukas, N. Sze, P. Klentrou and E. Tsiani, Ursolic Acid against Prostate and Urogenital Cancers: A Review of In Vitro and In Vivo Studies, *Int. J. Mol. Sci.*, 2023, **24**(8), 7414, DOI: 10.3390/ijms24087414.

68 Q. Sun, M. He, M. Zhang, S. Zeng, L. Chen, L. Zhou and H. Xu, Ursolic acid: A systematic review of its pharmacology, toxicity and rethink on its

 © 2026 The Author(s). Published by the Royal Society of Chemistry

pharmacokinetics based on PK-PD model, *Fitoterapia*, 2020, **147**, 104735, DOI: 10.1016/j.fitote.2020.104735.
69 S. Alfei, A. Schito and G. Zuccari, Considerable Improvement of Ursolic Acid Water Solubility by Its Encapsulation in Dendrimer Nanoparticles: Design, Synthesis and Physicochemical Characterization, *Nanomaterials*, 2021, **11**(9), 2196, DOI: 10.3390/nano11092196.
70 T. Zhao, C. Gu, J. Qi, J. Liu, Y. Wang, X. Chen, F. Guo and Y. Li, In vitro and in vivo performance of amorphous solid dispersions of ursolic acid as a function of polymer type and excipient addition, *J. Pharm. Pharmacol.*, 2024, **76**, 1584–1598, DOI: 10.1093/jpp/rgae125.
71 R. Latella, E. Calzoni, L. Urbanelli, G. Cerrotti, S. Porcellati, C. Emiliani, S. Buratta and B. Tancini, Isolation of Extracellular Vesicles from Agri-Food Wastes: A Novel Perspective in the Valorization of Agri-Food Wastes and By-Products, *Foods*, 2024, **13**(10), 1492, DOI: 10.3390/foods13101492.
72 S. Buratta, R. Latella, E. Chiaradia, A. Salzano, B. Tancini, R. Pellegrino, L. Urbanelli, G. Cerrotti, E. Calzoni, H. Alabed, *et al.*, Characterization of Nanovesicles Isolated from Olive Vegetation Water, *Foods*, 2024, **13**(6), 835, DOI: 10.3390/foods13060835.
73 M. Livshts, E. Khomyakova, E. Evtushenko, V. Lazarev, N. Kulemin, S. Semina, E. Generozov and V. Govorun, Isolation of exosomes by differential centrifugation: Theoretical analysis of a commonly used protocol, *Sci. Rep.*, 2015, **5**, 17319, DOI: 10.1038/srep17319.
74 T. Shieh, Y. Tseng, S. Hsia, T. Wang, W. Lan and Y. Shih, Optimization Protocol of the PEG-Based Method for OSCC-Derived Exosome Isolation and Downstream Applications, *Separations*, 2022, **9**(12), 435, DOI: 10.3390/separations9120435.
75 A. Sarasati, M. Syahruddin, A. Nuryanti, I. Ana, A. Barlian, C. Wijaya, D. Ratnadewi, T. Wungu and H. Takemori, Plant-Derived Exosome-like Nanoparticles for Biomedical Applications and Regenerative Therapy, *Biomedicines*, 2023, **11**(4), 1053, DOI: 10.3390/biomedicines11041053.
76 S. Fan, J. Chen, C. Tang, Q. Zhao, J. Zhang and Y. Qin, Edible plant extracellular vesicles: An emerging tool for bioactives delivery, *Front. Immunol.*, 2022, **13**, 1028418, DOI: 10.3389/fimmu.2022.1028418.
77 E. Bari, S. Perteghella, D. Di Silvestre, M. Sorlini, L. Catenacci, M. Sorrenti, G. Marrubini, R. Rossi, G. Tripodo, P. Mauri, *et al.*, Pilot Production of Mesenchymal Stem/Stromal Freeze-Dried Secretome for Cell-Free Regenerative Nanomedicine: A Validated GMP-Compliant Process, *Cells*, 2018, **7**(11), 190, DOI: 10.3390/cells7110190.
78 P. Lago, L. Rovati, L. Cantù and M. Corti, A quasielastic light scattering detector for chromatographic analysis, *Rev. Sci. Instrum.*, 1993, **64**, 1797–1802, DOI: 10.1063/1.1144013.
79 M. Sztucki, *SAXSutilities: a Graphical User Interface for Processing and Analysis of Small-Angle X-Ray Scattering Data (1.024)*, Zenodo, 2021.
80 C. Blanchet, A. Spilotros, F. Schwemmer, M. Graewert, A. Kikhney, C. Jeffries, D. Franke, D. Mark, R. Zengerle, F. Cipriani, *et al.*, Versatile sample environments and automation for biological solution X-ray scattering experiments at the P12 beamline (PETRA III, DESY), *J. Appl. Crystallogr.*, 2015, **48**, 431–443, DOI: 10.1107/S160057671500254X.
81 D. Franke, A. Kikhney and D. Svergun, Automated acquisition and analysis of small angle X-ray scattering data, *Nucl. Instrum. Methods Phys. Res., Sect. A*, 2012, **689**, 52–59, DOI: 10.1016/j.nima.2012.06.008.
82 G. Orlandi, E. Bari, L. Catenacci, M. Sorrenti, L. S egale, S. Faragò, M. Sorlini, C. R. Arciola, M. L. Torre and a. S. Perteghella, Polyphenols-Loaded Sericin Self-Assembling Nanoparticles: A Slow-Release for Regeneration by Tissue-Resident Mesenchymal Stem/Stromal Cells, *Pharmaceutics*, 2020, **12**(4), 381, DOI: 10.3390/pharmaceutics12040381.
83 H. Pagès, P. Aboyoun, R. Gentleman, S. DebRoy, *Efficient Manipulation of Biological Strings*, 2026, DOI: 10.18129/B9.bioc.Biostrings.
84 G. Raghava and G. Barton, Quantification of the variation in percentage identity for protein sequence alignments, *BMC Bioinf.*, 2006, **7**, 415, DOI: 10.1186/1471-2105-7-415.
85 B. Sherman, M. Hao, J. Qiu, X. Jiao, M. Baseler, H. Lane, T. Imamichi and W. Chang, DAVID: a web server for functional enrichment analysis and functional annotation of gene lists (2021 update), *Nucleic Acids Res.*, 2022, **50**, 216–221, DOI: 10.1093/nar/gkac194.
86 Y. Sangsen, K. Wiwattanawongsa, K. Likhitwitayawuid, B. Sritularak, P. Graidist and R. Wiwattanapatapee, Influence of surfactants in self-microemulsifying formulations on enhancing oral bioavailability of oxyresveratrol: Studies in Caco-2 cells and in vivo, *Int. J. Pharm.*, 2016, **498**, 294–303, DOI: 10.1016/j.ijpharm.2015.12.002.
87 H. Chang, A. Lee and J. Lee, Assessment of Digestion and Absorption Properties of 1,3-Dipalmitoyl-2-Oleoyl Glycerol-Rich Lipids Using an In Vitro Gastrointestinal Digestion and Caco-2 Cell-Mediated Coupled Model, *Molecules*, 2024, **29**(22), 5442, DOI: 10.3390/molecules29225442.
88 B. Srinivasan, A. Kolli, M. Esch, H. Abaci, M. Shuler and J. Hickman, TEER Measurement Techniques for In Vitro Barrier Model Systems, *JALA*, 2015, **20**, 107–126, DOI: 10.1177/2211068214561025.
89 M. Mocchi, E. Bari, G. Marrubini, A. F. Bonda, S. Perteghella, F. Tartara, F. Cofano, G. di Perna, L. Giovannelli, D. Mandracchia, *et al.*, Freeze-Dried Mesenchymal Stem Cell-Secretome Pharmaceuticalization: Optimization of Formulation and Manufacturing Process Robustness, *Pharmaceutics*, 2021, **13**(8), 1129, DOI: 10.3390/pharmaceutics13081129.
90 L. Giovannelli, E. Bari, C. Jommi, F. Tartara, D. Armocida, D. Garbossa, F. Cofano, M. L. Torre and L. Segale, Mesenchymal stem cell secretome and extracellular vesicles for neurodegenerative diseases: Risk-benefit profile and next steps for the market access, *Bioact. Mater.*, 2023, **29**, 16–35, DOI: 10.1016/j.bioactmat.2023.06.013.

© 2026 The Author(s). Published by the Royal Society of Chemistry

91 A. Kilasoniya, L. Garaeva, T. Shtam, A. Spitsyna, E. Putevich, B. Moreno-Chamba, J. Salazar-Bermeo, E. Komarova, A. Malek, M. Valero, *et al.*, Potential of Plant Exosome Vesicles from Grapefruit (Citrus x paradisi) and Tomato (Solanum lycopersicum) Juices as Functional Ingredients and Targeted Drug Delivery Vehicles, *Antioxidants*, 2023, **12**(4), 943, DOI: 10.3390/antiox12040943.

92 R. Lee, H. Ko, K. Kim, Y. Sohn, S. Min, J. Kim, D. Na and J. Yeon, Anti-melanogenic effects of extracellular vesicles derived from plant leaves and stems in mouse melanoma cells and human healthy skin, *J. Extracell. Vesicles*, 2020, **9**(1), 1703480, DOI: 10.1080/20013078.2019.1703480.

93 C. Stanly, M. Moubarak, I. Fiume, L. Turiák and G. Pocsfalvi, Membrane Transporters in Citrus clementina Fruit Juice-Derived Nanovesicles, *Int. J. Mol. Sci.*, 2019, **20**(24), 6205, DOI: 10.3390/ijms20246205.

94 X. Xi, M. Chen, S. Xia and R. Lu, Drug loading techniques for exosome-based drug delivery systems, *Pharmazie*, 2021, **76**, 61–67, DOI: 10.1691/ph.2021.0128.

95 E. Bertania, A. Modena, E. Bari, I. Miletto, D. Lim, L. Segale, G. Diana, A. Candiani, M. Sorlini and M. Torre, Silk fibroin nanoparticles coated with secretome-derived extracellular vesicles via GMP-ready microfluidics: a biomimetic carrier-in-carrier platform with preferential tumor cell internalization, *J. Mater. Chem. B*, 2026, **14**(38), 11767–11783, DOI: 10.1039/d6tb01053a.

96 E. Bertania, E. Bari, L. Segale, M. Sorlini and M. Torre, Advancing extracellular vesicles as drug delivery systems: a conceptual and prospective outlook on microfluidic methods for scalable, GMP-compliant drug loading, *Mater. Horiz.*, 2026, **13**, 8957–8978, DOI: 10.1039/d6mh01052k.

97 M. Hossain, V. De Leo, R. Tamborra, O. Laselva, C. Ingrosso, V. Daniello, L. Catucci, I. Losito, F. Sollitto, D. Loizzi, *et al.*, Characterization of anti-proliferative and anti-oxidant effects of nano-sized vesicles from Brassica oleracea L. (Broccoli), *Sci. Rep.*, 2022, **12**, 14362, DOI: 10.1038/s41598-022-17899-1.

98 S. Bruno, A. Paolini, V. D'Oria, A. Sarra, S. Sennato, F. Bordi and A. Masotti, Extracellular Vesicles Derived From Citrus sinensis Modulate Inflammatory Genes and Tight Junctions in a Human Model of Intestinal Epithelium, *Front. Nutr.*, 2021, **8**, 778998, DOI: 10.3389/fnut.2021.778998.

99 P. Nguyen, B. Liu, S. Zhang, J. Hao and J. Yu, Macropinocytosis and Fast Endophilin-Mediated Endocytosis Mediate Absorption of Garlic Chive-Derived Vesicle-like Nanoparticles in Human Intestinal Epithelial Cells, *Mol. Pharmaceutics*, 2025, **22**, 3935–3948, DOI: 10.1021/acs.molpharmaceut.5c00190.

© 2026 The Author(s). Published by the Royal Society of Chemistry